

1 **Wave Breaking Dissipation in a Young Wind Sea**

2 MICHAEL SCHWENDEMAN, * JIM THOMSON

Applied Physics Laboratory, University of Washington, Seattle, Washington

3 JOHANNES R. GEMMRICH

Department of Physics and Astronomy, University of Victoria, Victoria, British Columbia, Canada

* *Corresponding author address:* Michael Schwendeman, University of Washington 1013 NE 40th Street,
Box 355640 Seattle, WA 98105-6698
E-mail: mss28@u.washington.edu

4 ABSTRACT

5 Coupled *in situ* and remote sensing measurements of young, strongly-forced, wind waves
6 are applied to assess the role of breaking in an evolving wavefield. *In situ* measurements of
7 turbulent energy dissipation from wave-following “SWIFT” drifters and a tethered Dopbeam
8 system are consistent with wave evolution and wind input (as estimated using the Radiative
9 Transfer Equation). The Phillips breaking crest distribution is calculated using stabilized
10 shipboard video recordings and the Fourier-based method of Thomson and Jessup (2009),
11 with minor modifications. The resulting $\Lambda(c)$ are unimodal distributions centered around half
12 of the phase speed of the dominant waves, consistent with several recent studies. Breaking
13 rates from $\Lambda(c)$ increase with slope, similar to *in situ* dissipation. However, comparison
14 of the breaking rate estimates from the shipboard video recordings with the SWIFT video
15 recordings show that the breaking rate is likely underestimated in the shipboard video when
16 wave conditions are calmer and breaking crests are small. The breaking strength parameter,
17 b , is calculated by comparison of the fifth moment of $\Lambda(c)$ with the measured dissipation
18 rates. Neglecting recordings with inconsistent breaking rates, the resulting b data do not
19 display any clear trends and are in the range of other reported values. The $\Lambda(c)$ distributions
20 are compared with the Phillips (1985) equilibrium range prediction and previous laboratory
21 and field studies, leading to the identification of several inconsistencies.

22 1. Introduction

23 Wave breaking plays a primary role in the surface wave energy balance. The evolution of
24 a wave energy spectrum in frequency, $E(f)$, is governed by the Radiative Transfer Equation
25 (RTE),

$$\frac{\partial E(f)}{\partial t} + (c_g \cdot \nabla) E(f) = S_{in}(f) + S_{nl}(f) - S_{ds}(f) \quad (1)$$

26 where $S_{in}(f)$, $S_{nl}(f)$, and $S_{ds}(f)$ are the source terms corresponding to wind input, nonlin-
27 ear interactions, and dissipation, assuming minimal surface currents (Young 1999). Wave
28 breaking is thought to be the dominant mechanism for energy dissipation (Gemrich et al.
29 1994; Babanin et al. 2010b), though recent evidence suggests that non-breaking “swell” dis-
30 sipation may be significant when breaking is not present (Babanin and Haus 2009; Rogers
31 et al. 2012; Babanin and Chalikov 2012). Dissipation by breaking is widely considered to be
32 the least well-understood term and process in wave mechanics (Banner and Peregrine 1993;
33 Thorpe 1995; Melville 1996; Duncan 2001; Babanin 2011). In particular, there have been
34 only a few field studies that quantify the wave energy lost to whitecaps in deep water.

35 Much of the energy lost during wave breaking is dissipated as turbulence in the ocean
36 surface layer. Several studies (Kitaigorodskii et al. 1983; Agrawal et al. 1992; Anis and
37 Moum 1995; Terray et al. 1996) have shown a layer of enhanced dissipation under breaking
38 waves. Below this enhanced layer, measurements tend to approach the expected “law of
39 the wall” scaling associated with flow over a solid, flat, boundary. Gemrich and Farmer
40 (2004) correlated enhanced dissipation with breaking events, suggesting that dissipation in
41 this surface layer corresponds to energy lost from breaking waves. Thus, measurements of
42 turbulent dissipation can be used as a proxy estimate of breaking dissipation. These are
43 lower bound estimates, however, as some wave energy is also spent on work done in the
44 submersion of bubbles (as much as 50% according to Loewen and Melville 1991).

45 Gemrich (2010) measured turbulent dissipation in the field using a system of three
46 high-resolution pulse-coherent Sontek Dopbeam acoustic Doppler sonars, profiling upwards

47 into the wave crest above the mean water line. Gemmrich (2010) found that turbulence was
 48 enhanced particularly in the crest, even more so than previous observations. Thomson (2012)
 49 achieved a similar result with wave-following “SWIFT” drifters, which measure turbulent
 50 dissipation from near the surface to a half meter depth with a pulse-coherent Aquadopp HR
 51 acoustic Doppler profiler. Both these studies estimate dissipation rate using the second-order
 52 structure function, $D(z, r)$, as described in Section 2 and in Wiles et al. (2006).

53 Using laboratory measurements, Duncan (1981, 1983) related the speed of a steady break-
 54 ing wave to its energy dissipation rate. Towing a hydrofoil through a long channel at a
 55 constant speed and depth, Duncan (1981) determined that the rate of energy loss followed
 56 the scaling

$$\epsilon_l \propto \frac{\rho_w c^5}{g} \quad (2)$$

57 where ϵ_l is the energy dissipation per crest length, ρ_w is the water density, g is gravitational
 58 acceleration, and c is the speed of the towed hydrofoil. Melville (1994) examined data
 59 from previous laboratory experiments of unsteady breaking (Loewen and Melville 1991) and
 60 noted an additional dependence of dissipation on wave slope, as also suggested in Duncan
 61 (1981). Drazen et al. (2008) used a scaling argument and a simple model of a plunging
 62 breaker to hypothesize that dissipation depends on wave slope to the 5/2 power. They
 63 compiled previous data and made additional laboratory measurements and found roughly
 64 the expected dependence on slope.

65 In parallel with Duncan’s work, Phillips (1985) introduced a statistical description of
 66 breaking, $\Lambda(c, \theta)$, which is defined as the distribution of breaking crest lengths per area as a
 67 function of speed, c , and direction, θ . Thus the total length of breaking crests per area is

$$L_{total} = \int_0^\infty \int_0^{2\pi} \Lambda(c, \theta) c d\theta dc. \quad (3)$$

68 The scalar distribution, $\Lambda(c)$, is often used in place of the full directional distribution. It
 69 can be found by integrating over all directions in broad-banded waves or by using the speed
 70 in the dominant direction in sufficiently narrow-banded wavefields. The breaking rate, or

71 breaker passage rate, is the frequency that an actively breaking crest will pass a fixed point
 72 in space. The breaking rate can be calculated from the first moment of $\Lambda(c)$,

$$R_\Lambda = \int c\Lambda(c)dc. \quad (4)$$

73 Phillips (1985) used Duncan’s scaling to propose a relation for the total breaking-induced
 74 dissipation from the $\Lambda(c)$ distribution,

$$S_{ds,\Lambda} = \int \epsilon(c)dc = \frac{b\rho_w}{g} \int c^5\Lambda(c)dc \quad (5)$$

75 where b is a “breaking strength” proportionality factor and $\epsilon(c)$ is the spectral dissipation
 76 function in phase speed.

77 In addition, Phillips (1985) hypothesized that at wavenumbers sufficiently larger than
 78 the peak, a spectral equilibrium range exists such that wind input, nonlinear transfers, and
 79 dissipation are all of the same order and spectral shape. Phillips (1985) proposed a spectral
 80 form of the dissipation function within the equilibrium range,

$$\epsilon(c) = 4\gamma\beta^3 I(3p)\rho_w u_*^3 c^{-1} \quad (6)$$

81 where

$$I(3p) = \int_{-\pi/2}^{\pi/2} (\cos \theta)^{3p} d\theta \quad (7)$$

82 is a directional weight function, γ , β , and p are constants, and u_* is the wind friction velocity.
 83 Thus, Phillips derived that, within the equilibrium range, $\Lambda(c)$ should follow c^{-6} and be given
 84 by

$$\Lambda(c) = (4\gamma\beta^3)I(3p)b^{-1}u_*^3 g c^{-6}. \quad (8)$$

85 The $\Lambda(c)$ formulation is well-suited to remote sensing methods, which have shown promise
 86 in the field because of their ability to capture more breaking events than *in situ* point
 87 measurements. Early remote studies such as Ding and Farmer (1994) and Gemmrich and

88 Farmer (1999) calculated wave breaking statistics without using $\Lambda(c)$. Later, the Duncan-
89 Phillips formulation was recognized as a potential means to relate remote-sensed whitecap
90 measurements to dissipation. Phillips et al. (2001) produced the first field observations of
91 $\Lambda(c)$, using backscatter from radar data. Melville and Matusov (2002) used digital video
92 taken from an airplane to calculate $\Lambda(c)$. Gemmrich et al. (2008) also calculated $\Lambda(c)$ from
93 digital video, in this case from the Research Platform *FLIP*. The studies of Kleiss and Melville
94 (2010), Kleiss and Melville (2011), and Romero et al. (2012) all used $\Lambda(c)$ measurements from
95 airplane video during the Gulf of Tehuantepec Experiment (GOTEX).

96 The results of Thomson and Jessup (2009) and Thomson et al. (2009) are of particular
97 relevance to the present work. Thomson and Jessup (2009) introduced a Fourier-based
98 method for processing shipboard video data into $\Lambda(c)$ distributions. The Fourier method
99 has the advantage of increased efficiency and robust statistics compared to conventional
100 time-domain crest-tracking methods. This method was validated alongside an algorithm
101 similar to the one used in Gemmrich et al. (2008). Thomson et al. (2009) presented the
102 results of the Fourier method for breaking waves in Lake Washington and Puget Sound.

103 Despite the widely varying wave conditions, experimental methods, and processing tech-
104 niques, a number of similar characteristics can be seen in the $\Lambda(c)$ results from these recent
105 studies. With the exception of Melville and Matusov (2002), all of the $\Lambda(c)$ show a uni-
106 modal distribution with a peak at speeds roughly half the dominant phase speed. Melville
107 and Matusov (2002) instead calculated a monotonically decreasing $\Lambda(c)$, but had limited
108 resolution and used an assumption that the rear of breaking crests was stationary. Kleiss
109 and Melville (2011) demonstrated that the rear of a whitecap is not in fact stationary, and
110 the differing result from Melville and Matusov (2002) could be reproduced in their data by
111 imitating the study's video processing method. The peaked distribution differs from the c^{-6}
112 shape predicted by Phillips (1985), though most studies note tails in $\Lambda(c)$ approaching c^{-6} at
113 high speeds. These speeds, however, are not generally within the equilibrium range used to
114 arrive at Eq. (8). Plant (2012) recently suggested that the unimodal $\Lambda(c)$ distributions are

115 produced by an interference pattern of dominant wind waves, moving at speeds slightly less
 116 than the group velocity and resulting in large wave slopes during constructive interference.
 117 Another similarity in recent $\Lambda(c)$ studies is the dominance of infrequent, fast-moving white-
 118 caps in the distribution of the fifth moment $c^5\Lambda(c)$, which is used to calculate dissipation.
 119 Plots of $c^5\Lambda(c)$ often show significant values up to the highest speed bin for which they are
 120 calculated.

121 Knowledge of b is crucial to the remote calculation of dissipation. Values of b from the
 122 field have spanned four orders of magnitude, from 3.2×10^{-5} in Gemmrich et al. (2008) to
 123 1.7×10^{-2} in Thomson et al. (2009). One issue appears to be the different choices made in
 124 processing $\Lambda(c)$, in particular defining the whitecap speed and length. Kleiss and Melville
 125 (2011) reviewed the methods of Gemmrich et al. (2008) and Kleiss and Melville (2010) and
 126 noted a 300% difference in b resulting from their differing speed and length definitions.

127 Another problem is uncertainty over the nature of b . In introducing the concept, Phillips
 128 (1985) treated b as a constant, however, as noted above, the studies of Melville (1994)
 129 and Drazen et al. (2008) indicate at least one secondary dependence on wave slope. Wave
 130 slope can be represented in a number of ways from the wave spectrum, $E(f)$. In Banner
 131 et al. (2000), the breaking probability of dominant waves was found to correlate best with
 132 significant peak steepness, $H_p k_p / 2$ where

$$H_p = 4 \left\{ \int_{0.7f_p}^{1.3f_p} E(f) df \right\}^{1/2}, \quad (9)$$

133 and k_p is the peak wavenumber, calculated from f_p with the deep-water dispersion relation.
 134 Another measure of steepness can be calculated using the significant wave height, H_s , in
 135 place of H_p . Banner et al. (2002) showed that for a range of wave scales, the breaking
 136 probability was related to the azimuthal-integrated spectral saturation,

$$\sigma = \int_0^{2\pi} k^4 \Phi(k, \theta) d\theta = \frac{(2\pi)^4 f^5 E(f)}{2g^2} \quad (10)$$

137 where Φ is the wavenumber spectrum, k is the wavenumber magnitude, and θ is the direction.
 138 Breaking was found to occur above a threshold value of σ , with the breaking probability

139 increasing roughly linearly with σ above this threshold. The saturation spectrum is related
140 to wave mean square slope (mss) through

$$\text{mss} = \iint k^2 \Phi(k, \theta) k dk d\theta = \int \frac{2\sigma}{f} df. \quad (11)$$

141 Romero et al. (2012) used the $\Lambda(c)$ distributions from Kleiss and Melville (2010) to
142 calculate a spectral $b(c)$ based on the Drazen et al. (2008) wave slope results applied to the
143 saturation spectrum. In the present study, bulk b values are calculated for an evolving wave
144 field to investigate possible trends with wave slope or steepness. Calculation of b or $b(c)$
145 requires $\Lambda(c)$ and a separate measurement of the breaking dissipation. The use of turbulent
146 dissipation as an estimate of breaking dissipation was first utilized in Thomson et al. (2009).
147 In the absence of *in situ* measurements, Gemmrich et al. (2008) and Romero et al. (2012)
148 used indirect estimates of dissipation from wind measurements and wave spectra [i.e., the
149 residual of Eq. (1)]. A disadvantage of this indirect method is that uncertainties in the wind
150 parameterizations and wave measurements can lead to errors in dissipation estimates.

151 In the following sections, *in situ* and remote techniques are used to measure dissipation
152 from breaking, wave evolution, and $\Lambda(c)$ in a young sea with strong wind forcing. In Section 2,
153 the field experiment is described and the methods are summarized. In Section 3, the results
154 are presented and *in situ* measurements are compared with $\Lambda(c)$ estimates. In Section 4, the
155 findings are discussed and sources of uncertainty in the data are addressed.

156 2. Methods

157 a. Collection of Wind and Wave Data

158 Observations were made in the Strait of Juan de Fuca (48°12' N 122°55' W), north of
159 Sequim, Washington, from February 12-19, 2011. Measurements were taken onboard the
160 *R/V Robertson* and from two free-floating “SWIFT” (Surface Wave Instrument Float with
161 Tracking) drifters. The roughest conditions were observed during the days of February 14

162 and 15, in which a winter storm produced southerly winds of 9-18 m s⁻¹. On these days,
163 the *R/V Robertson* was set on a drogue and allowed to drift across the Strait (downwind)
164 at approximately 2 km hr⁻¹.

165 Wave measurements were made from the two wave-following SWIFT drifters. These
166 Lagrangian drifters are described in detail in Thomson (2012). They were equipped with
167 a QStarz BT-Q1000eX, 5 Hz GPS logger and accelerometer, 2 MHz Nortek Aquadopp HR
168 pulse-coherent Acoustic Doppler Current Profiler (ADCP) with 4 Hz sampling and 4 cm
169 bin size, Go-Pro Hero digital video camera, and Kestral 4500 anemometer. The SWIFTS
170 were released from the *R/V Robertson* and generally drifted at similar speeds, thus staying
171 within approximately 1 km of the ship. Wave frequency spectra and associated parameters
172 are estimated from the orbital velocities measured by Doppler speed-resolving GPS loggers
173 onboard the freely-drifting SWIFTS, using the method of Herbers et al. (2012).

174 Wind measurements were made from a shipboard sonic anemometer (RM Young 8100),
175 at a height of 8.9 m above the water surface, as well as from the SWIFTS at 0.9 m. The
176 wind friction velocity u_* is estimated using the inertial dissipation method as described in
177 Yelland et al. (1994). Thomson (2012) measured the drift of the SWIFTS due to wind drag
178 at speeds roughly 5% of the wind speed. Using this estimate to remove wind drift, the tidal
179 surface currents can be inferred as the residual of the SWIFT displacements, and were below
180 0.6 m s⁻¹ throughout the experiment.

181 Figure 1 shows the tracks of the ship and SWIFTS for the two days of interest. In
182 addition, bulk wind and wave quantities are shown as a function of fetch. Wave height
183 and period increased along track, and wind speed increased slowly on both days. Wind
184 friction velocity, however, did not vary as much as wind speed during the two days. The
185 non-dimensional wave age, calculated as $c_p U_{10}^{-1}$ where c_p is the peak phase speed, only briefly
186 exceeds 0.5 at the beginning of each day, when the wind is lowest. Thus, the observed waves
187 constitute a young, highly-forced, pure wind sea.

188 In addition, wind measurements are used from two nearby stations operated by the

189 National Data Buoy Center (NDBC), with locations shown in Figure 1a. The anemometer
 190 at Smith Island (NDBC #SISW1) is located at 17.1 m above the site elevation, or 32.3 m
 191 above the mean sea level. The 3-meter discus buoy offshore of the Dungeness Spit (NDBC
 192 #46088) makes wind measurements from a height of 5 m above sea level. Additionally, the
 193 Dungeness buoy outputs frequency-directional wave spectra.

194 Figure 2 shows the evolution of the SWIFT-derived wave frequency spectrum, $E(f)$,
 195 binned by fetch every 500 m. It has been widely observed that the spectrum approaches a
 196 region of the form f^{-n} for high frequencies, with the most commonly cited values of n being
 197 $n = 5$ (as in Phillips 1958; Hasselmann et al. 1973) and $n = 4$ (as in Toba 1973; Donelan
 198 et al. 1985), both of which are shown in Figure 2. In deriving Eq. (6), Phillips (1985) used
 199 the Toba (1973) form $E(f) \propto u_* g f^{-4}$, so this comparison is of particular interest. Except
 200 for briefly after the peak and in the higher frequencies ($f \geq 1$ Hz), the spectra follow f^{-5}
 201 much better than f^{-4} . When colored by u_* in Figure 2b, however, the curves do appear to
 202 sort in the tail as expected from the Toba spectrum.

203 *b. In Situ Estimates of Energy Dissipation*

204 The rate of energy dissipation via wave breaking, S_{ds} , is estimated using *in situ* measure-
 205 ments of turbulent velocity profiles $u(z)$ in a reference frame moving with the wave surface.
 206 This is done from two SWIFT drifters, as described above and in Thomson (2012) and, in-
 207 dependently, from a wave-following platform equipped with Sontek Dopbeam pulse-coherent
 208 acoustic Doppler profilers and tethered to the ship with a 30 m rubber cord. This Dopbeam
 209 system is discussed further in Gemmrich (2010).

210 The volumetric dissipation rate $\epsilon_{vol}(z)$ is calculated by fitting a power law to the observed
 211 turbulent structure function,

$$D(z, r) = \langle (u'(z) - u'(z + r))^2 \rangle = A(z)r^{2/3} + N \quad (12)$$

212 where z is measured in the wave-following reference frame (i.e. $z = 0$ is the water surface),

213 r is the lag distance between measurements (corresponding to eddy scale), $A(z)$ is the fitted
 214 parameter, and N is a noise offset. Assuming isotropic turbulence in the inertial subrange,
 215 the eddy cascade goes as $r^{2/3}$ and the volumetric turbulent dissipation rate is related to each
 216 fitted $A(z)$ by

$$\epsilon_{vol}(z) = C_v^{-3} A(z)^{3/2} \quad (13)$$

217 where C_v is a constant equal to 1.45 (Wiles et al. 2006). Integrating the dissipation profiles
 218 over depth gives a total dissipation rate,

$$S_{ds,SWIFT} = \rho_w \int_{-0.6}^0 \epsilon_{vol}(z) dz \quad (14)$$

219 where z is measured from the instantaneous water surface ($z = 0$) to the bottom bin depth
 220 of 0.6 m. The structure function is averaged over 5 minute intervals before calculating the
 221 dissipation. In addition, profiles of $\epsilon_{vol}(z)$ are removed if the $r^{2/3}$ fit does not account for at
 222 least 80% of the variance or if A is similar in magnitude to N (see Thomson 2012). Figure
 223 3 shows the evolution of the dissipation profiles and total dissipation with fetch. Profiles
 224 of dissipation deepen, and the overall magnitude increases, as waves grow along fetch and
 225 breaking increases. In Thomson et al. (2009), a persistent, constant background dissipation
 226 of 0.5 W m^{-2} was noted in both Lake Washington and Puget Sound in the absence of
 227 visible breaking. This is consistent with the SWIFT measurements here, thus a 0.5 W m^{-2}
 228 average background dissipation level is subtracted from SWIFT and Dopbeam dissipation
 229 measurements in the following sections.

230 *c. Video Observations of Wave Breaking*

231 Wave breaking observations were made from a video camera mounted above the *R/V*
 232 *Robertson* wheelhouse, at 7 m above the mean water level, aimed off the port side of the
 233 ship. With the drogue set from the stern, the port side view was an undisturbed wavefield.
 234 The video camera was equipped with a 1/3" Hi-Res Sony ExView B&W CCD. The data

235 (eight-bit grayscale, 640×480 pixel, NTSC) was sampled at 30 Hz and later subsampled
236 to 15 Hz. The lens had a 92° horizontal field of view and was oriented downward at an
237 incidence angle of approximately 70 degrees, giving a pixel resolution of 10-40 cm in the
238 analyzed region. The video was stabilized in the vertical and azimuthal (pitch and yaw)
239 directions with a pan-tilt mounting system (Directed Perception PTU-D100). This video
240 data is used to estimate the breaking rates and the $\Lambda(c)$ distributions.

241 Additionally, video taken from the SWIFTs is examined to produce independent esti-
242 mates of the rate of breaking at a much higher pixel resolution (since the SWIFT cameras
243 are only 0.9 m from the surface). Unfortunately, the batteries on the SWIFT Go-Pro cam-
244 eras expired after around 2 hours, so only early conditions on each day could be examined.
245 A total of eleven 30-minute video recordings from the SWIFTs are processed. SWIFT break-
246 ing rates are calculated by counting the number of breaking waves passing the SWIFT and
247 dividing by the duration of the recording (30 minutes). The counting is subjective, as the
248 SWIFT video is too motion-contaminated to produce accurate automated results. Only
249 clear whitecaps that broke prior to reaching the SWIFT with crest lengths larger than the
250 diameter of the SWIFT hull (0.3 m) are counted.

251 Shipboard video data are processed according to Thomson and Jessup (2009), as sum-
252 marized below. Four minor modifications to this method are detailed in Appendix A.

253 The analysis begins with the rectification of camera pixels to real-world coordinates using
254 the method of Holland et al. (1997). Here the x and y directions are taken as the along-
255 ship and cross-ship directions, respectively. A portion of the image, roughly $15 \text{ m} \times 20 \text{ m}$
256 and no closer than 15 m from the ship is extracted and interpolated to a uniform grid of
257 2^n points. The camera position was remotely reset periodically, as it was prone to drift in
258 the azimuth at rate of about 5° per minute. Short video windows of 5 to 10 minutes were
259 chosen for analysis to avoid these resets and ensure statistical stationarity of the breaking
260 conditions. This window length is comparable to those shown in Kleiss and Melville (2010)
261 although the field of view is significantly smaller (roughly 0.2 km^2 in their study). The

262 uncertainty introduced from these small windows is addressed in Section 4. This field of
263 view is sufficient to capture complete crests for the conditions observed. The resulting pixel
264 resolution is around 0.25 m (cross wave) by 0.075 m (along wave).

265 The rectified video is broken up into segments of 1024 frames (68.3 seconds) with 25%
266 overlap. Sequential images are subtracted to create differenced images, which highlight the
267 moving features of the video, most prominently the leading edge of breaking waves. The
268 breaking crests are further isolated when the differenced images are thresholded to binary
269 images, $I(x, y, t)$ (see Appendix A for choice of threshold). This procedure was originally
270 described in Gemmrich et al. (2008). Two examples of the progression from raw image to
271 binary are shown in Figure 4 along with SWIFT images from the same times. These images
272 demonstrate the range of breaking conditions seen during the experiment. The left images
273 are representative of the calmer conditions towards the beginning of both days' experiments,
274 with small and transient breaking crests. The right images are representative of the rough
275 conditions later in each day (after drifting out to a larger fetch), with larger and more
276 vigorous breaking crests.

277 After thresholding, a three-dimensional fast Fourier Transform (FFT) is performed on
278 the binary shipboard video data, $I(x, y, t)$, which is then filtered in wavenumber to isolate the
279 crest motion. Integration over the k_y (along-crest) component produces a two-dimensional
280 frequency-wavenumber spectrum, $S(k_x, f)$, as shown in Figure 2a of Thomson and Jessup
281 (2009). Directional distributions of breaking could not be calculated from this dataset be-
282 cause of the shipboard camera configuration. With a camera height of 7 m and incidences
283 angles of $60^\circ - 70^\circ$, changes in sea surface elevation due to the waves themselves can manifest
284 as movement in the lateral, or y , direction. This corrupts the y -velocities and prevents the
285 calculation of an accurate directional distribution. Following the method of Chickadel et al.
286 (2003), the frequency-wavenumber spectrum is transformed to a speed-wavenumber spec-
287 trum using $c = f/k_x$, and the Jacobian $|\partial f/\partial c| = |k_x|$ preserves the variance in the spectrum.
288 The speed spectrum is calculated by integrating over the wavenumber, $S(c) = \int S(k_x, c) dk_x$.

289 This speed spectrum has the shape of the $\Lambda(c)$ distribution, but it must be normalized
 290 to have the correct magnitude. The normalization follows from a direct calculation of the
 291 average breaking length per unit area, L_{total} ,

$$L_{total} = dy \frac{\sum I(x, y, t)}{NA}, \quad (15)$$

292 where dy is the length of the pixels along the crests, $\sum I(x, y, t)$ is the number of breaking
 293 pixels, N is the number of frames, and A is the area of the field of view. Thus, $\Lambda(c)$ is
 294 calculated as

$$\Lambda(c) = L_{total} \frac{S(c)}{\int S(c)dc}, \quad (16)$$

295 directly following Thomson and Jessup (2009). Removal of bias in Eq. (16) is described in
 296 Appendix A.

297 Nine cases of 5 to 10 minutes were used from the video record to calculate $\Lambda(c)$ distri-
 298 butions during the experiment. Table 1 shows the time, fetch, duration, and bulk wind and
 299 wave values from these cases. Figure 5 shows the resulting $\Lambda(c)$ as a function of dimensional
 300 speed and normalized speed, c/c_p , and colored by mss. These distributions are qualitatively
 301 similar to those from Gemmrich et al. (2008), Thomson et al. (2009), and Kleiss and Melville
 302 (2010), with a peaked shape centered around approximately $0.5c_p$. As expected, the magni-
 303 tude of $\Lambda(c)$ increases with mss. In addition, a region of roughly c^{-6} is visible at high speeds,
 304 similar to the theoretical shape described in Eq. (8).

305 **3. Analysis & Results**

306 *a. Fetch Dependence*

307 The *R/V Robertson* and SWIFT measurements of winds and waves are highly dependent
 308 on fetch, because of the drift mode for data collection. The fetch dependence is directly
 309 related to wave slope and thus wave breaking (Banner et al. 2002). Here, these measurements

310 are compared with the idealized case of fetch-limited wave growth, in which a wind of
 311 constant magnitude and direction blows out from from a straight coastline.

312 Figure 6 compares the drifting measurements of wind speed, direction, and wave height
 313 from the *R/V Robertson* and SWIFTs with fixed measurements from the two nearby National
 314 Data Buoy Center (NDBC) stations (see locations in Figure 1). The NDBC measurements
 315 are converted to U_{10} by assuming a logarithmic profile with a representative drag coefficient,
 316 $C_D = 1.2 \times 10^{-3}$ (Large and Pond 1981). There is significant spatial heterogeneity in the
 317 wind speed measurements. In particular, on February 14, the wind measured from the ship
 318 increases dramatically with increasing fetch, while both NDBC wind speed measurements
 319 are roughly constant. The ship wind speeds converge to roughly the same 17 m s^{-1} value
 320 as measured from the NDBC stations when the ship reaches a fetch similar to the NDBC
 321 stations. It is likely that some of the increase in measured wind speed with fetch is due to the
 322 sharp transition in roughness at the coastline and the resulting adjustment of the boundary
 323 layer (Smith and Macpherson 1987). The February 15 wind data, measured only at fetches
 324 longer than 12 km, matches the NDBC measurements much better. As expected, the wave
 325 height at the NDBC buoy stays approximately constant in response to the roughly steady
 326 winds, whereas the SWIFT wave heights grow in time due to the increasing fetch along a
 327 drift track.

328 For ideal fetch-limited waves, Kitaigorodskii (1962) argued that the wave field could be
 329 fully characterized by the fetch, X , gravitational acceleration, g , and a scaling wind speed.
 330 Thus empirical “laws” have often been sought for wave energy and frequency growth with
 331 fetch (e.g. CERC 1977; Donelan et al. 1985; Dobson et al. 1989; Donelan et al. 1992). The
 332 scaled variables take the form:

$$\hat{x} = \frac{gX}{U_{10}^2}, \quad \hat{e} = \frac{g^2 E_0}{U_{10}^4}, \quad \hat{f} = \frac{U_{10} f_p}{g} \quad (17)$$

333 where E_0 is the wave variance, and f_p is the frequency at the peak of the wave spectrum.
 334 The wind speed at a 10 m reference height, U_{10} , is most often used as the scaling wind speed
 335 as it is easily measured in the field. Young (1999) consolidated a number of the proposed

336 fetch relations into two power laws with a range of coefficients. Figures 7a,b compare this
337 current data set against Young’s empirical relations, using 500-meter along-fetch averaging.

338 The non-dimensionalized data are highly sensitive to the choice of appropriate wind
339 speed, particularly for February 14 where the wind grows from 10 to 19 m s⁻¹ along the
340 fetch. Three wind speed scalings are compared in Figures 7a,b, using: a constant time-
341 averaged wind speed, an instantaneous wind speed, and a linear fetch-averaged wind speed
342 (à la Dobson et al. 1989). Based on the NDBC wind data alone, a constant U_{10} scaling
343 might seem appropriate. In fact, scaling with the constant wind agrees much better with
344 the empirical fetch laws than either fetch-dependent wind speed scaling. In addition, wave
345 conditions at the Dungeness Spit buoy (NDBC #46088) are also plotted in Figure 7a,b, and
346 there is good agreement with the fetch laws. This is a notable contrast of reference frames:
347 the fixed station suggests a fetch-limited wave field, while the drifting measurements do not.

348 Two additional parameters are plotted against non-dimensional fetch in Figure 7c,d. One
349 is mean square slope, mss , calculated from the wave spectra as in Eq. (11), which is as-
350 sociated with the likelihood of wave breaking (Banner et al. 2002). Wave slope increases
351 logarithmically with non-dimensional fetch on February 14. On February 15, mss also in-
352 creases with fetch, but the waves are in the mid-range of the previous day. These trends are
353 similar for a number of alternative slope or steepness parameters (not shown). Also plotted
354 is the drag coefficient, C_D , calculated as a ratio of u_*^2 and U_{10}^2 . These measurements are inde-
355 pendent, since u_* is calculated from wind turbulent dissipation (Yelland et al. 1994) rather
356 than mean wind speed. At very short fetches, the drag is notably higher than the remainder
357 of the data, which again is evidence of the adjustment of the atmospheric boundary layer to
358 the land-water edge. At longer fetches, drag is in the expected range of $1-2 \times 10^{-3}$ and shows
359 a mild increasing trend along fetch (and thus with steepness).

360 This field experiment exhibits two of the features — an irregular coastline and wind
361 heterogeneity — which prompted Donelan et al. (1992) to write that “perhaps it is time to
362 abandon the idea that a universal power law for non-dimensional fetch-limited growth rate is

363 anything more than an idealization.” It is likely that the ambiguous comparison of the data
 364 with the established fetch laws is a result of both the non-ideal winds and the rapid change
 365 of the atmospheric boundary layer at very short fetches, which itself is a result of changes in
 366 roughness due to waves. The observed fetch dependence suggests a wave field that rapidly
 367 evolves in the first few kilometers, then grows more gradually as the fetch lengthens. This
 368 is consistent with the *in situ* breaking dissipation estimates, which increase sharply from 0
 369 to 5 km fetch, then vary only moderately from 5 to 15 km fetch (Figure 3).

370 *b. Energy Fluxes*

371 As discussed in Section 1, the evolution of ocean surface waves is governed by the Radia-
 372 tive Transfer Equation (RTE). Here, we calculate each of the terms in a bulk RTE, which is
 373 integrated over all frequencies,

$$\frac{\partial E}{\partial t} + c_g \cdot \nabla E = S_{in} - S_{ds}. \quad (18)$$

374 such that the nonlinear term is dropped as it does not change the total energy in the system,
 375 only the distribution of the energy within the spectrum. By considering the total energy
 376 budget, we can diagnose the wave evolution along fetch and assess the estimates of wave
 377 breaking dissipation. Figure 8 shows the estimates of all terms in Eq. (18).

378 In general, both local growth and advective flux of wave energy [the left two terms in Eq.
 379 (18)] occur in response to wind forcing. Without a large array of wave measurements, it is
 380 impossible to explicitly separate the two growth terms. One approximation is to assume a
 381 stationary wavefield, such that $\partial E/\partial t = 0$ and all wave growth is due to advection of wave
 382 energy at the group velocity. The ambiguous comparison with empirical fetch laws in Figure
 383 7, however, indicates that a stationary assumption may not be appropriate. An additional
 384 issue is noise in the wave energy measurements, which causes large variability in the growth
 385 terms when using finite differences to approximate the derivatives. This is problematic even
 386 when the spectra are averaged over 500-meter spatial bins as in Figure 2.

387 To treat both the issues of stationarity and measurement noise in the left-hand side
 388 of Eq. (18), large-scale estimates are made separately based on daily linear regressions of
 389 wave energy with fetch and time (i.e., regressions of ΔE vs. Δx and Δt). The first case
 390 is equivalent to the stationary assumption, where all growth during the experiment is due
 391 to advection of wave energy. In the second case, the wave energy is assumed constant in
 392 fetch, such that all the change in wave energy is due to local, temporal growth. Tables 2
 393 and 3 show the results of $\partial E/\partial t$ and $\partial E/\partial x$ for February 14 and 15, including R^2 values
 394 and 95% confidence intervals. As noted above, neither of these cases describes perfectly the
 395 true evolution of wave energy, which is actually a combination of both terms. However, they
 396 lead to a range of possible values

$$\min\left(\overline{\frac{\partial E}{\partial t}}, c_g \overline{\frac{\partial E}{\partial x}}\right) \leq \left(\frac{\partial E}{\partial t} + c_g \frac{\partial E}{\partial x}\right) \leq \left(\overline{\frac{\partial E}{\partial t}} + c_g \overline{\frac{\partial E}{\partial x}}\right) \quad (19)$$

397 where overbars indicate the daily averages from Tables 2 and 3. Here, c_g is calculated from
 398 the peak frequency using the deep-water dispersion relation.

399 Figure 8b shows this range of values from Eq. (19). Apart from the small change in
 400 c_g , this estimate does not capture possible variations in growth within each day, but the
 401 R^2 values shown in Tables 2 and 3 show that a constant linear approximation is reasonable
 402 (minimum R^2 of 0.82, mean of 0.90). A more conservative range would use the outer values
 403 of the 95% confidence intervals of the regressions.

404 The wind input function in Eq. (18) is parameterized using the wind stress, $\rho_a u_*^2$, and
 405 an effective phase speed, c_{eff} , such that

$$S_{in} = \rho_a c_{eff} u_*^2, \quad (20)$$

406 as described in Gemmrich et al. (1994). There is significant uncertainty in the choice of c_{eff} .
 407 Terray et al. (1996) found c_{eff} to be somewhat less than the peak phase speed and show a
 408 dependence on wave age, albeit with much scatter. Figure 6 from Terray et al. (1996) shows
 409 values of c_{eff} ranging between roughly $0.3c_p$ and $0.7c_p$ for our range of $u_*c_p^{-1}$. Thus, the

410 range of values for the wind input term is

$$0.3\rho_a c_p u_*^2 \leq S_{in} \leq 0.7\rho_a c_p u_*^2. \quad (21)$$

411 The resulting wind input range is shown in Figure 8a.

412 With Eqs. (18), (19) and (21), the range of possible dissipation values during the ex-
413 periment can be computed and compared with the measured turbulent dissipation from the
414 SWIFTs and the Dopbeams. This comparison is shown in Figure 8c. An additional black
415 line is shown in each of the panels, corresponding to $c_{eff} = 0.5c_p$ and a stationary wavefield
416 ($\partial E/\partial t = 0$). The measured results fall within the estimated range from the energy balance
417 for all but a few points during the experiment. Where this range would include negative
418 values of dissipation, including all of February 15, it has been limited to zero.

419 Whereas the stationary RTE dissipation roughly matches the turbulent dissipation on
420 February 14, it underestimates the turbulent dissipation on February 15, consistent with an
421 overestimate of $\partial E/\partial x$. This is related to the intercept of the linear regression in fetch (see
422 Table 2). If the growth were perfectly linear in fetch, this intercept would be expected to be
423 near zero (no wave energy at zero fetch). On February 14, this is indeed the case, with the
424 intercept at less than 1 km. On February 15, however, the intercept is on the order of 10
425 km, indicating that either the growth is not linear along fetch or the growth is not steady.
426 This is consistent with Figure 7, where for all wind speed scalings, wave energy on February
427 15 grows faster than the expected trend.

428 Figure 8 shows that bulk dissipation estimates from the RTE are similar to turbulent
429 dissipation measurements, both of which show dissipation increasing along fetch (and thus
430 with wave slope), especially at very short fetches. At larger fetches, the RTE dissipation
431 continues to increase, more so than the relatively flat turbulent dissipation measurements. It
432 is likely that the *in situ* turbulence measurements of dissipation are biased low, because some
433 wave energy is lost during whitecapping to work in submerging bubbles (Loewen and Melville
434 1991). Thus, if bubble effects account for an increasing fraction of the total dissipation as
435 the waves grow, the turbulence measurements would increasingly underestimate the total

436 dissipation, as seen particularly on February 14. This is important context for the comparison
437 of *in situ* results with breaking statistics from the video data.

438 *c. Breaking Rate*

439 Breaking rates from the ship-based $\Lambda(c)$ distributions and from the manual SWIFT-based
440 breaker counts are shown in Figure 9a. Both measurements show an overall positive trend
441 with wave slope, as expected, but the dynamic range and shape of the trends are significantly
442 different. Whereas the SWIFT values vary from only 16-58 hr^{-1} , the shipboard breaking
443 rates vary over two orders of magnitude, from 3-229 hr^{-1} . Unfortunately, SWIFT video
444 cameras ran out of battery power prior to reaching the maximum breaking conditions. The
445 actual overlap is with the first three shipboard observations from February 14 and the first
446 two from February 15. In general, the SWIFT breaking rates are larger than the shipboard
447 measurements, and thus the overall trend with mss is decreased. The low breaking rates from
448 the shipboard video are likely biased by insufficient pixel resolution, and these values are
449 plotted with open symbols to reflect low confidence in these points (see Figure 9 and again
450 later in Figure 10). The two estimates are relatively close for the maximum overlapping
451 point (68 hr^{-1} from shipboard vs. 58 hr^{-1} from the SWIFT), indicating that these estimates
452 may be consistent when the waves are larger and steeper (i.e. at larger mss in Figure 9 and
453 larger fetch in Figure 8).

454 The SWIFT breaking rates imply that the shipboard video regularly misses breaking
455 waves during less steep conditions, when whitecaps are short-crested and the foam they
456 produce is short-lived. As shown with examples in Figure 4, the small-scale breaking seen
457 frequently in the SWIFT video (Figure 4c) is barely visible in the shipboard video (Figure 4b)
458 during calmer conditions. Moreover, many uncounted wave crests appear to break without
459 producing foam, but are visible from the SWIFT due to the layer of water sliding down
460 their front face or ripples forming near the crest. These small-scale breakers are similar
461 to “microbreakers”, which are a well-known phenomenon (e.g. Jessup et al. 1997). As the

462 waves evolve, however, the character of the breaking changes. Large, vigorous whitecaps
 463 start to replace the small, transient breaking events seen at the shorter fetches, and evidence
 464 of microbreaking becomes less apparent. These larger whitecaps (Figure 4f) are more visible
 465 from the shipboard video (Figure 4d) and the breaking rates converge for later times.

466 The higher breaking rates from the SWIFT video during calmer conditions are consistent
 467 with the *in situ* turbulent dissipation estimates. As shown in Figure 9, both breaking and
 468 dissipation increase approximately one order of magnitude as waves evolve and steepen. This
 469 implies that each wave dissipates roughly the same amount of energy during breaking, such
 470 that more breaking produces more dissipation. The breaking rates from the shipboard video,
 471 by contrast, increase much more dramatically than the dissipation estimates, which would
 472 imply that each breaking wave contributes less dissipation as the wave field evolves. This is
 473 both physically unlikely and contrary to the Duncan-Phillips theory, where the dissipation
 474 rate of a breaking wave is proportional to c^5 times its crest length, with a proposed additional
 475 *positive* dependence on wave slope (Melville 1994; Drazen et al. 2008). Thus, only ship-
 476 based video recordings from the rougher conditions (filled symbols of Figure 9a) are used in
 477 assessing the $\Lambda(c)$ and b results.

478 *d. Breaking Strength Parameter*

479 The value of the bulk breaking parameter b is calculated from

$$b = \frac{S_{ds}}{\rho_w g^{-1} \int c^5 \Lambda(c) dc}, \quad (22)$$

480 using each of the four measures of dissipation, S_{ds} , from Figure 8. These calculated b values
 481 are shown as a function of mss, wave age, and significant steepness in Figure 10. Only one
 482 SWIFT was in the water during the two February 15 video segments, thus there is one less
 483 b value for these $\Lambda(c)$. The independent variables use the average of mss, c_p , U_{10} , and H_s
 484 within a 500 m region around each $\Lambda(c)$ calculation. As in Figure 9a, values that are biased
 485 by insufficient pixel resolution are shown with open symbols.

486 In addition, data is included from measurements made in Lake Washington, WA, in 2006
 487 and Puget Sound, WA, in 2008, originally reported in Thomson et al. (2009). Whereas in
 488 Thomson et al. (2009), a constant b was obtained via regression of $\int c^5 \Lambda(c) dc$ to the measured
 489 dissipation, here individual values of b are calculated. Apart from the updates to the Fourier
 490 method detailed in Appendix A, the $\Lambda(c)$ methodology is similar between the datasets. The
 491 comparison of b with wave age and steepness is in part motivated by the desire to compare
 492 across these datasets, as the spectra from the earlier measurements are insufficient quality
 493 to calculate mean square slope.

494 As expected, the b values are affected by undercounting small whitecaps in less steep
 495 seas. The biased points, shown in open symbols, have dramatic trends of decreasing b with
 496 increasing wind forcing (described by inverse wave age, U_{10}/c_p) and increasing wave slope
 497 (using mean square slope, mss, and peak wave steepness, $H_s k_p/2$). The Thomson et al.
 498 (2009) data show these same trends, suggesting the same biasing effect. This trend may be
 499 expected in any $\Lambda(c)$ study with insufficient sampling of small-scale breaking.

500 The remaining unbiased values, shown in solid symbols, have b grouped around a constant
 501 on the order of 10^{-3} . No statistically significant trends are present. In particular, the increase
 502 in b with wave slope shown in Drazen et al. (2008) is not observed, though the range of wave
 503 slopes here is quite limited relative to Drazen et al. (2008). Thus, as in Phillips et al. (2001),
 504 Gemmrich et al. (2008), and Thomson et al. (2009), the best estimate of b for this study is a
 505 constant range over the experimental conditions. The five unbiased $\Lambda(c)$ distributions, each
 506 paired with four S_{ds} estimates, result in an ensemble of 20 points. Amongst this set, the
 507 mean b value is 3.2×10^{-3} , with a standard deviation of 1.5×10^{-3} . This range is highlighted
 508 in gray in Figure 10 and is applicable for waves with $\text{mss} \geq 0.031$ or $H_s k_p/2 \geq 0.19$.

509 Figure 10 also shows these b values relative to other recent studies. Clearly, they are lower
 510 than the average b of $8 - 20 \times 10^{-3}$ reported from the Puget Sound and Lake Washington
 511 data in Thomson et al. (2009), which is a direct result of the under-sampling of small
 512 breakers in the previous study. The experimental results of Banner and Pierson (2007)

513 found laboratory waves of slope $0.12 - 0.17$ to have b values between $1 - 12 \times 10^{-4}$. The
 514 laboratory study of Drazen et al. (2008) did not measure breaking waves with slopes less
 515 than 0.22 , but the power law fit through their data predicts b values between $3.1 - 5.3 \times 10^{-3}$
 516 for the range of steepness shown here. The Romero et al. (2012) $b(c)$ are of $O(10^{-2} - 10^{-4})$
 517 for speeds below c_p . Gemmrich et al. (2008) give a range of b that is significantly lower,
 518 $3.2 \times 10^{-5} \leq b \leq 10.1 \times 10^{-5}$. Phillips et al. (2001) calculate b ranging from $7 - 13 \times 10^{-4}$.

519 The b values reported from field studies are sensitive to the upper limit of integration
 520 in Eq. (22). This integral can be unbounded, with significant contributions to the total
 521 area coming from sporadic, extremely rare, or nonexistent breaking above the spectral peak.
 522 This problem is not unique to this study, though it can be exacerbated by the Fourier
 523 method as discussed in Appendix A. The results of Romero et al. (2012) suggest a solution
 524 to this dilemma. The bulk b calculated in Eq. (22) represents all speeds, in contrast to the
 525 spectral $b(c)$ from Romero et al. (2012). The Romero et al. (2012) model and data shows,
 526 however, that above c_p a precipitous drop in breaking strength should be expected, due to
 527 the decreased saturation of these waves. Thus, the upper limit of the integration in Eq. (22)
 528 is taken to be c_p . In effect, this amounts to a $b(c)$ model where $b(c)$ is constant for $c \leq c_p$
 529 and zero for $c > c_p$.

530 4. Discussion

531 *a. Importance of Small-scale Breaking*

532 It has long been accepted that foam-based breaker detection methods are incapable of
 533 measuring microbreakers. However, microbreaking is often treated as an afterthought, or an
 534 effect which is important only at the very short wave scales. This study leads to two impor-
 535 tant considerations regarding microbreakers. First, the distinction between whitecaps and
 536 microbreakers is not straightforward. Comparison of SWIFT and shipboard video reveals
 537 that many breaking waves which are visible from the SWIFTs do not show up in the ship-

538 board video. These are not true microbreakers as they do aerate the surface, however they
539 are not visible from the ship due to their short crest length, short duration, and low contrast
540 of foam produced. This phenomenon does not appear to be limited to the high-frequency
541 waves; rather, it seems to be a broadband effect based more on the overall wave steepness
542 (as given by the integrated mean square slope).

543 Second, these breaking waves appear to have a biasing effect. As the breaking becomes
544 stronger, large whitecaps replace, rather than simply add to, the smaller-scale breaking
545 events. If this biasing effect is indeed important, it is not unique to this study. Clearly,
546 the Lake Washington and Puget Sound data from Thomson et al. (2009) shown in Figure
547 10 display evidence of this bias as well. Kleiss and Melville (2011) compiled breaking rates
548 from five datasets which show a very similar range of values to those shown here in Figure 9,
549 after normalizing by the wave period. Babanin et al. (2010b) compared the empirical $\Lambda(c)$
550 function proposed by Melville and Matusov (2002) with a numerical dissipation function and
551 showed that b needed to change over four orders of magnitude to reproduce the appropriate
552 dissipation. Gemmrich et al. (2008) is notable both for their low estimates of b ($\sim 3 -$
553 10×10^{-5}) and the high resolution of their video (pixel sizes of 3.2×10^{-2} m). This is
554 consistent with the proposition that small-scale breaking waves are not resolved in most
555 other field measurements. Whereas Drazen et al. (2008) showed that the large range of b
556 values reported in laboratory measurements could be somewhat explained by differences in
557 wave steepness, we propose that the range in b reported from field measurements is large
558 due to the biasing effect of small-scale breaking and/or the ability of different video systems
559 to resolve small breakers.

560 Infrared (IR) imaging may improve remote sensing of small-scale breaking, by detecting
561 the disturbance in the thermal boundary layer even when foam is not visible (Jessup et al.
562 1997). Jessup and Phadnis (2005) made IR measurements of $\Lambda(c)$ for laboratory microbreak-
563 ers, but similar measurements can be challenging to make in the field. Recently, Sutherland
564 and Melville (2013) made the first field measurements of $\Lambda(c)$ with stereo IR cameras. Such

565 measurements are essential to quantify the dynamics of small-scale breakers and the overall
566 effect of small-scale breaking on wave evolution.

567 *b. Sensitivity and Error in b*

568 The largest source of uncertainty in the measured $\Lambda(c)$ is the omission of microbreakers
569 and small-scale whitecaps. However, there are several other sources of uncertainty in the b
570 estimates, which are shown in Figure 11, using the S_{ds} values from SWIFT 1 (red symbols
571 in 10).

572 One potential source of error is from the relatively short video recordings (5-10 minutes)
573 used to determine each $\Lambda(c)$. Synthetic data were created to determine the errors of the
574 Fourier method caused by short recordings. The synthetic data is a binary time series
575 resembling thresholded, natural, crests. The speed of the breaking crests follow a normal
576 distribution centered around 3 m s^{-1} , for similarity with the field data. Noise, in the form of
577 randomness in the speed of each synthetic pixel, is added to avoid “ringing” in the Fourier
578 result. In natural data there is always sufficient noise to avoid ringing. Because the speed
579 and crest length of the synthetic breakers is prescribed, the true $\Lambda(c)$ distribution is easily
580 calculated and compared with the curve obtained from the Fourier method. For each video
581 recording from the field, 50 runs of synthetic data were analyzed using the same configuration,
582 breaking rate, and duration. An example of the family of resulting $\Lambda(c)$ distributions is
583 shown in Figure 12a for the data point of February 14, 21:34 UTC (see Table 1), along with
584 the input Gaussian distribution. Clearly, significant errors from the true $\Lambda(c)$ are possible
585 when using such limited data. The resulting uncertainty in b from propagating these errors
586 through in the integral of $c^5\Lambda(c)dc$ is shown in Figure 11a. As expected, the uncertainty
587 is greatest in the data with the sparsest breaking (higher b), which is already known to be
588 biased by the pixel resolution. Within the unbiased data, the errors introduced by the short
589 windows are small relative to the scatter of the data.

590 The calculation of b is also subject to uncertainty from S_{ds} . In Figure 10, b values

591 corresponding to four independent measurements of S_{ds} are shown. The uncertainty in
592 the inferred S_{ds} from the Radiative Transfer Equation is shown in Figure 8. The SWIFT
593 and Dopbeam uncertainty is discussed in the Thomson (2012). One source of error is in
594 the power law fit of the structure function in Eq. (12). Lower and upper bounds of the
595 SWIFT dissipation are propagated through the calculations using the root-mean-square
596 error (RMSE) of the power law fit. The resulting b error bars for SWIFT 1 are shown in
597 Figure 11b. These errors are comparatively small relative to the uncertainties from $\Lambda(c)$.

598 The sensitivity of b to choices made in the $\Lambda(c)$ processing are shown in Figure 11c-e.
599 For example, the threshold value used to generate the binary video frames (see Appendix A)
600 controls the number of pixels identified as “breaking crests.” The effect on b of adjusting this
601 threshold by $\pm 20\%$ is shown Figure 11c. The error bars associated with this manipulation
602 are roughly uniform and extend approximately half an order of magnitude. Similarly, varying
603 the upper limit $c = c_p$ in the integration of $c^5 \Lambda(c) dc$ by $\pm 20\%$ shifts the b results by roughly
604 a half order of magnitude, as shown in Figure 11d.

605 Finally, there is some disagreement over the correct speed to assign each breaking event.
606 In Phillips’s theory, c refers to the phase speed of the breaking wave. It has been observed,
607 however, that the speed of the whitecap is actually somewhat less than the phase speed.
608 Laboratory experiments (Rapp and Melville 1990; Banner and Pierson 2007; Stansell and
609 MacFarlane 2002), show a possible linear relationship between the two speeds of the form
610 $c_{brk} = \alpha c$, where c is the true phase speed, c_{brk} is the observed speed of the whitecap, and
611 α ranges from 0.7 to 0.95. Moreover, Kleiss and Melville (2011) showed that the speed of
612 advancing foam in breaking waves tends to slow over the course of a breaking event. This is
613 consistent with the laboratory study of Babanin et al. (2010a), which showed a shortening
614 and slowing in waves breaking from modulational instability. Since the Fourier method
615 includes contributions from speeds throughout the duration of breaking, it distributes the
616 contributions from a single breaking event to a number of speed bins. This interpretation
617 of breaker speed, however, may be contrary to the original definition of the $\Lambda(c)$ function

618 by Phillips (1985) (Mike Banner, personal communication). The effect on $\Lambda(c)$ of these
619 two modifications to the assigned breaking speed is similar – both serve to shift breaking
620 contributions to higher phase speeds.

621 Using synthetic data, we have determined that the Fourier method $\Lambda(c)$ centers on the
622 average speed of the breaking wave. Thus, for crests slowing to 55% of their maximum speed,
623 as in Kleiss and Melville (2011), the effect is similar to using $\alpha = 0.775$. The implications
624 of this difference are most apparent in the fifth moment calculation, where using $\alpha = 0.7$
625 (the most extreme literature value) increases the magnitude of $c^5\Lambda(c)dc$ by $\alpha^{-6} = 850\%$, as
626 shown in Figure 11e. Adjusting to maximum breaker speeds, our final b estimates would
627 be $O(10^{-4})$, rather than the $O(10^{-3})$ we obtain with average breaker speeds. Thus, the
628 slowing effect is thus similar in extreme to the bias of insufficient pixel resolution – either
629 can increase the inferred b by over an order of magnitude.

630 *c. Comparison with Phillips’s Relation*

631 Phillips (1985) introduced the concept of a spectral “equilibrium range,” for which the
632 nonlinear energy transfers, wind input, and dissipation are in local equilibrium. This theory
633 explained the consistent f^{-4} shape noted by Toba (1973) and others in the tail of the
634 frequency spectrum. The theory modified Phillips’s earlier (1958) theory of a region of
635 constant saturation, which led to an f^{-5} slope in the spectral tail. The equilibrium range
636 has usually been assumed to begin at $k > 2k_p$, or, equivalently, $c < 0.7c_p$ (e.g. Kleiss and
637 Melville 2010). Romero and Melville (2010) noted a transition in their wavenumber spectra
638 from $k^{-5/2}$ (equivalent to f^{-4}) to k^{-3} (f^{-5}) at higher wavelengths, and proposed that this
639 marked a transition from equilibrium to saturation ranges. The frequency spectra in Figure
640 2 appear to largely follow f^{-5} for frequencies above the peak, perhaps implying a narrow
641 equilibrium range. This is consistent with the wave age dependency proposed in Romero
642 and Melville (2010), as these are young, highly forced waves.

643 Within the equilibrium range, Phillips (1985) predicted $\Lambda(c)$ to follow the c^{-6} form of

Eq. (8), based on the derived dissipation term in that region [Eq. (6)]. It has often been noted that $\Lambda(c)$ resembles c^{-6} at speeds beyond its peak (e.g. Thomson et al. 2009), as is also shown in Figure 5. However, these speeds are not generally within the equilibrium range, as shown in Figure 13a,b. In Figure 13a, the frequency spectrum corresponding to each $\Lambda(c)$ curve is plotted as a function of phase speed using the dispersion relation. Figure 13b shows that at speeds where equilibrium may exist, $c < 0.7c_p$, $\Lambda(c)$ does not show the predicted form. Instead, a peaked curve similar to many recent studies is observed. This result implies either a flaw in Phillips’s equilibrium range spectral dissipation function [Eq. (6)], significant errors in estimates of $\Lambda(c)$, or deviations from Duncan’s c^5 scaling of breaking dissipation [Eq. (2)].

As described above, our wave spectra do not show a distinct equilibrium range, characterized by an f^{-4} slope in the tail. Since Eq. (6) is only expected to hold within the equilibrium range, it could be argued that this is the source of the discrepancy in the shape of $\Lambda(c)$. The peaked $\Lambda(c)$ shape, however, has been measured in a wide variety of wave conditions. It is unlikely that this particular source of error would be universal in the literature data. Another possible issue is the lack of microbreaking measurements here and in most previous field studies. One exception is the recent study by Sutherland and Melville (2013), which used stereo IR video to improve detection of small-scale breaking. Their $\Lambda(c)$ agree well with visible video measurements at high speeds, but extended the c^{-6} region to lower speeds. This presents the possibility that the peaked $\Lambda(c)$ within the equilibrium range noted here and throughout the literature is due to the prevalence of microbreaking in this range. More such IR measurements would be helpful for evaluating this argument.

The final potential cause of the difference between the measured $\Lambda(c)$ and Phillips’s prediction is in the use of Duncan’s c^5 scaling of dissipation. One way to implicitly modify Duncan’s c^5 scaling is through a spectral $b(c)$ or $b(k)$. In studying wave breaking in the Gulf of Tehuantepec Experiment (GOTEX), Romero et al. (2012) proposed two such models of

670 b ,

$$b_1(k) = A_1(\sigma^{1/2} - B_T^{1/2})^{5/2} \quad (23)$$

671 and

$$b_2(k) = A_2(\tilde{\sigma}^{1/2} - \tilde{B}_T^{1/2})^{5/2} \quad (24)$$

672 where σ is the azimuthal-integrated spectral saturation in wavenumber [Eq. (10)], $\tilde{\sigma}$ is
673 saturation normalized by the directional spreading, and A_1 , A_2 , B_T , and \tilde{B}_T are coefficients
674 fit to their data. These models are based on the results of Banner and Pierson (2007) and
675 Drazen et al. (2008) showing a 5/2 power law dependence on wave slope. In Figure 13c, the
676 spectral $b_1(k)$ is plotted for our data using $A_1 = 4.5$ and $B_T = 9.3 \times 10^{-4}$, which Romero
677 et al. (2012) calculate for $\alpha = 1$ (i.e. assuming whitecap speed equals the underlying wave
678 phase speed) and using the Janssen (1991) wind input function. The saturation spectra are
679 calculated as in Eq. (10). The model $b(k)$ is then converted to $b(c)$ using the deep-water
680 phase speed $c = \sqrt{g/k}$.

681 Two important features of the Romero et al. (2012) $b_1(c)$ are worth noting. Above c_p ,
682 $b_1(c)$ decreases dramatically due to a drop-off in σ . This means that the effective exponent
683 in the proposed c^5 Duncan scaling is actually much less than 5 in this region. This result
684 was used to justify the upper limit of c_p in the integration of $c^5\Lambda(c)$ in the previous section.
685 Below c_p , $b_1(c)$ is essentially flat, thus it does not explain the discrepancy with Eq. (8)
686 in this region. Similarly, Romero et al. (2012) noted that their measured $b(c)$ were much
687 higher than their model $b_1(c)$ at these low speeds. For this reason, they do not extend their
688 calculated b to speeds less than 4.5 m s⁻¹. This region is shown with dotted lines in Figure
689 13, and makes up the entire potential equilibrium range for our waves.

690 The $b(c)$ models from Romero et al. (2012) are based on the premise that the c^5 scaling of
691 Duncan need only be modified to include a secondary dependence on wave slope. However,
692 there are a number of other possible reasons for the apparent deviations from the original
693 c^5 scaling. First, Duncan's relation was derived for steady breakers caused by a towed

694 hydrofoil. Since ocean breaking waves are fundamentally unsteady, time derivatives may
695 play an important role in the dissipation scaling. Although the c^5 scaling has been applied to
696 unsteady breaking in Melville (1994) and Drazen et al. (2008) with an additional dependence
697 on wave slope, these laboratory breakers do not necessarily simulate natural whitecaps.
698 Ocean waves break primarily due to modulational instability, whereas laboratory waves
699 are usually induced to break by linear superposition (Babanin 2011). In addition, three-
700 dimensional wave effects (i.e., the short-crestedness that is a signature of whitecaps) are not
701 well simulated in flume experiments. Another characteristic of natural waves which is not
702 included in laboratory experiments is the influence of short wave modulation by the peak
703 wave orbitals. Thomson and Jessup (2009) and Kleiss and Melville (2011) both corrected
704 for this effect in their $\Lambda(c)$ calculations, but found that the change was minimal, thus it was
705 not performed here. However, it is still not clear what effect this modulation has on the c^5
706 scaling, and it has been proposed that the Duncan scaling is only applicable for the spectral
707 peak waves where there is no modulation (Babanin 2011). This, again, is not where the
708 Phillips (1985) equilibrium form is expected.

709 The original Duncan (1981) experiments need revisiting in light of these issues. The
710 basis for scaling dissipation by c^5 comes from a momentum argument, where the change in
711 momentum is related to the tangential component of the weight of the breaking region, per
712 unit crest length, $gA \sin \theta$. Here θ is the wave slope and A is the cross-sectional area of the
713 breaking region. Duncan (1981) showed experimentally that for the steady breaking waves,

$$gA \sin \theta = \frac{0.015}{g \sin \theta} c^4. \quad (25)$$

714 Calculation of a rate of energy loss from the above force requires an additional velocity term,
715 so it is natural to again use c , resulting in the ultimate c^5 scaling of the dissipation rate.
716 However, Eq. (25) has to our knowledge never been verified for unsteady ocean breaking
717 waves. Confirmation of the original Duncan (1981) results for ocean whitecaps is a necessary,
718 and so far missing, step to using $c^5 \Lambda(c)$ to measure breaking dissipation. If the cross-sectional
719 area of active breaking, A , does not scale as c^4 , the results of Duncan and Phillips cannot

720 be applied to obtain dissipation in the field.

721 Additionally, the use $c^5\Lambda(c)$ to calculate a spectral dissipation, $\epsilon(c)$, as in Phillips (1985)
722 or Romero et al. (2012) relies on the assumption of spectrally local breaking dissipation.
723 This means that all the dissipation from a breaking wave is assigned to a single spectral
724 component, or a small range of spectral components if a variable c is tracked throughout the
725 breaking event. Phillips (1985) noted that this may only be applicable within the equilibrium
726 range. It has since been shown that breaking of the dominant waves causes dissipation of
727 the waves at scales smaller than the peak waves (e.g. Young and Babanin 2006). Recent
728 updates to spectral dissipation models (Ardhuin et al. 2010; Rogers et al. 2012) have used
729 a so-called “cumulative term” to reproduce this effect. Thus, it is possible that some of the
730 dissipation unaccounted for at small speeds here and in Romero et al. (2012) is in fact caused
731 by breaking at larger scales.

732 *d. Non-breaking Dissipation*

733 Another consideration in dissipation estimation is the effect of non-breaking wave dissi-
734 pation, often called “swell dissipation.” In recent years, the observation that in waves where
735 no breaking takes place there is still appreciable dissipation of wave energy has motivated
736 the search for other mechanisms of wave dissipation (Babanin 2011). The most promising
737 of these so far has been that when the wave orbital velocities achieves a certain threshold
738 Reynolds number, the orbital motion transitions from laminar to turbulent, and this tur-
739 bulence dissipates wave energy (Babanin and Haus 2009). The relevance for this study is
740 that the total dissipation is used in calculating b , where it would be more appropriate to use
741 only the breaking contribution to the dissipation. The magnitude of this swell dissipation is
742 still not clear, especially in waves where breaking is also present. Babanin (2011) used lab-
743 oratory measurements from Babanin and Haus (2009) and observations of swell dissipation

744 from Ardhuin et al. (2009) to estimate the average volumetric swell dissipation as

$$\epsilon_{vol}(z) = 0.002ku_{orb}^3 \quad (26)$$

745 where k is the wavenumber and u_{orb} is the wave orbital velocity. Babanin and Chalikov
746 (2012) calculated swell dissipation in numerical simulations of a fully-developed wavefield,
747 and found that the volumetric dissipation scaled as

$$\epsilon_{vol}(z) = 3.87 \times 10^{-7} H_s^{1/2} g^{3/2} \exp \left[0.506 \frac{z}{H_s} + 0.0057 \left(\frac{z}{H_s} \right)^2 \right]. \quad (27)$$

748 Eq. (26) gives dissipation rates of $1 - 10 \times 10^{-4} \text{ m}^2 \text{ s}^{-3}$, while Eq. (27) is of order $10^{-5} \text{ m}^2 \text{ s}^{-3}$.
749 Compared with the measured dissipation of $\epsilon_{vol} \sim 10^{-3} \text{ m}^2 \text{ s}^{-3}$, these two estimates differ
750 on whether this mechanism is an appreciable source of dissipation in this system, or a very
751 minor source. In truth, both estimates are still largely speculative, since swell dissipation
752 has so far not been measured in the presence of breaking (Babanin and Chalikov 2012). The
753 use of total dissipation in place of breaking dissipation in studies of $\Lambda(c)$ such as this one
754 may lead to an overestimation of b , as breaking dissipation is less than the total dissipation.
755 The magnitude of this bias depends on the relative importance of the breaking and swell
756 terms.

757 5. Conclusions

758 Video and *in situ* measurements waves during a winter storm in the Strait of Juan de Fuca
759 show a strong fetch dependence in wave spectral evolution and wave breaking. Heterogeneity
760 in the wind forcing prevents drifting wave measurements from conforming to fetch-limited
761 scaling laws, although nearby measurements at fixed stations are marginally consistent with
762 fetch-limited scaling laws. The discrepancy is most exaggerated at short fetches where
763 atmospheric drag is high and wave growth is rapid.

764 Estimates of wave breaking dissipation inferred from turbulence measurements are consis-
765 tent with estimates from a wave energy budget using the Radiative Transfer Equation (RTE).

766 There is a strong correlation between wave breaking dissipation and the mean square slope,
767 mss, of the waves, both of which increase along fetch.

768 Video-derived breaking rates and breaking crest distributions $\Lambda(c)$ also increase with
769 mss. However, during calmer conditions, estimates of breaking rates differ between high-
770 resolution video recorded on SWIFT drifters and low-resolution video recorded from a ship.
771 This bias is attributed to under-counting the small breakers, and thus the $\Lambda(c)$ results
772 during calmer conditions are not used. From the remaining $\Lambda(c)$ results, the bulk breaking
773 parameter b is estimated to be constant through the experiment at around 10^{-3} . Error
774 analysis indicates that video collection and processing details, such as pixel resolution and
775 breaker speed definition, can alter b by an order of magnitude (at least).

776 Compared to recent literature, these $\Lambda(c)$ results are similar in shape and magnitude.
777 However, we suggest that many b values from recent field experiments, notably those of
778 Thomson et al. (2009), are likely biased by subtleties of video collection and processing.
779 We also suggest that the c^5 scaling for energy dissipation from the original Duncan (1981)
780 laboratory experiments is of limited validity for application to whitecaps observed in the
781 field, especially in the c^{-6} equilibrium range envisioned by Phillips (1985). This is related to
782 recent efforts to determine a spectral $b(c)$ (e.g. Romero et al. 2012), which implicitly alter
783 the c^5 scaling.

784 *Acknowledgments.*

785 Thanks to the field crews from University of Washington Applied Physics Lab: Joe Tal-
786 bert, Alex de Klerk, and Captain Andy Reay-Ellers. Funding provided by the National
787 Science Foundation, the Charles V. “Tom” and Jean C. Gibbs Endowed Presidential Fellow-
788 ship in Environmental Engineering, and the Seattle Chapter of the ARCS Foundation.

789

790

791

Fourier Method Modifications

792

Modifications to the Fourier method of Thomson and Jessup (2009) are described below.

793

a. Calculation of Incidence Angle from Horizon

794

795

796

797

798

799

The camera incidence angle was not constant, because of the slow drift and periodic resetting of the stabilized pan and tilt. The stabilized pan and tilt adequately removed wave motions (e.g. ship roll at periods of a few seconds) from the video recordings, but contamination from lower period motions is evident in the raw video data. To remove these motions, the horizon in the undistorted image (i.e., after lens “barrel” distortion is removed) is used as a constant reference. First, the angle above horizontal is calculated as

$$\beta = \frac{y_{top} - y_{horizon}}{y_{top} - y_{bottom}} \times 69^\circ \quad (\text{A1})$$

800

801

where 69° is the total vertical field of view and y is in pixels. Then, the incidence angle is calculated simply as

$$\theta = 90 - 69^\circ/2 + \beta \quad (\text{A2})$$

802

803

804

In practice, the horizon is manually identified in four images every 30 seconds and the average value of the resulting incidence angle is used for all images in that 30 seconds. The incidence angle is essential for rectifying the video data to real-world coordinates (Holland et al. 1997).

805

b. Difference Threshold

806

807

Choosing an accurate binary threshold to identify breaking crests is critical to obtaining the correct $\Lambda(c)$ distribution. Differences in lighting and foam conditions make it difficult

808 to determine a single threshold criterion. In Thomson and Jessup (2009), a threshold based
 809 on a multiple of the image standard deviation is used, with similar results over a range of
 810 conditions. In the present study, however, the wider range of conditions necessitate a more
 811 adaptable method. Thus, the modification of a technique described in Kleiss and Melville
 812 (2011) is used, which is based on the cumulative complementary distribution of pixels

$$W(i_t) = 1 - \int_{-\infty}^{i_t} p(i) di, \quad (\text{A3})$$

813 where $p(i)$ is the probability density function of the subtracted brightnesses. The main
 814 difference from Kleiss and Melville (2011) is the use of the differenced images rather than
 815 the raw frames. As shown in Kleiss and Melville (2011) Figure 3, $W(i_t)$ decreases from 1 to 0
 816 as i_t increases, and shows a distinct tail at high i_t when breaking is present. This signature is
 817 also present when using differenced images. The tail is seen clearly in the second derivative
 818 of the log of $W(i_t)$, L'' . As noted by Kleiss and Melville (2011), taking the threshold as the
 819 beginning of this deviation (i.e. maximum L'') produces a number of false positives in their
 820 data. To obtain better signal-to-noise, they settle on a threshold value where L'' falls to
 821 20% of its maximum value. The same threshold is applied here, after manually confirming
 822 that this is near the point when thresholding stops excluding more residual foam and begins
 823 cutting off the edges of true breaking crests.

824 *c. Constant Signal-to-Noise Filter*

825 Thomson and Jessup (2009) describe the need to isolate the significant bands around the
 826 peak in the wavenumber-frequency spectrum when transforming to $S(c)$ to prevent noise
 827 from biasing the speed signal (page 1667). To this end, Thomson and Jessup (2009) restrict
 828 the integration from $S(k_y, f)$ to $S(k_y, c)$ to the points where the value of $S(k_y, f)$ is greater
 829 than 50% of the peak of $S(k_y)$. This process was slightly modified after examining the
 830 accuracy of the Fourier method with synthetic data. It was found that significant gains in
 831 accuracy could be made by using an integration cut-off that did not vary with wavenumber,

832 as shown in Figure 14. The true $\Lambda(c)$ curve in Figure 14 is the Gaussian function used as
 833 the input distribution to the synthetic data. The “original” $\Lambda(c)$ comes from the Fourier
 834 method as described in Thomson and Jessup (2009). For the “modified” curve, values
 835 from wavenumbers or frequencies less than 0.2 s^{-1} or m^{-1} are removed as they contain a
 836 high density of noise. Next, a constant cut-off 5% of the absolute maximum value of the
 837 remaining spectrum is used in the limits of integration around the significant band. The
 838 comparison is also shown on logarithmic axes in Figure 14b. This plot confirms the gains in
 839 accuracy of the modified filter at both the low and high speeds tails of the distribution, but
 840 also shows a general issue with the Fourier method at high speeds. Whereas time-domain
 841 calculations of $\Lambda(c)$ contain zeros at high speeds where no observations are measured, the
 842 Fourier method contains small, non-zero values related to the noise floor in the spectrum.
 843 These small contributions may be amplified when taking higher moments of $\Lambda(c)$. Therefore,
 844 some caution must be used in integrating $c^5\Lambda(c)$ to large c in Eq. (5), which is discussed in
 845 Section 3.

846 *d. Width/Speed Bias*

847 A central assumption in the normalization of $\Lambda(c)$ by L_{total} described above is that the
 848 width of the breaking crests is exactly one pixel, so that all $\sum I(x, y, t)$ pixels contribute to
 849 the length of the crest. However, breaking that occurs at speeds faster than one pixel per
 850 frame, $c > \Delta x/\Delta t$, will produce crests in the binary image of width

$$n = \frac{c}{\Delta x/\Delta t}, \quad (\text{A4})$$

851 where Δx is the pixel width in the breaking direction and Δt is the separation between
 852 frames (here, 0.0667 seconds). Evidence of this effect is shown in Figure 15a, where the
 853 average horizontal advancement of crests is plotted against their average width, weighted by
 854 crest size. These variables are well-correlated, and the relation follows closely the one-to-one
 855 line predicted by Eq. (A4). To correct for the associated bias of additional pixels with

856 fasters crests, the FFT normalization of Thomson & Jessup (2009) is modified with the ratio
 857 of $\Delta x/\Delta t$ to obtain

$$\Lambda(c) = L_{total} \frac{\Delta x/\Delta t}{c} \frac{S(c)}{\int S(c)dc}. \quad (\text{A5})$$

858 From Eq. (4), the breaking rate can be calculated from the first moment of $\Lambda(c)$. In
 859 addition, the breaking rate can be calculated directly from the binary images as

$$R_I = \frac{\sum I(x, y, t)}{n_x n_y N \Delta t}, \quad (\text{A6})$$

860 where n_x and n_y are the number of pixels in x and y . Carrying through the integration in
 861 Eq. (4) with the modified $\Lambda(c)$ from Eq. (A5) results in an equivalent expression as Eq.
 862 (A6). Thus, in effect the width modification amounts to rescaling $\Lambda(c)$ to match the direct
 863 breaking rate, R_I . Figure 15b compares R_Λ from the original $\Lambda(c)$ distribution and from
 864 the width corrected $\Lambda(c)$ with the direct breaking rate, R_I . The linear trend in the original
 865 results indicates that the bias is small and linear. The final results show identically equal
 866 values of R_I and R_Λ , as required by this normalization.

REFERENCES

- 869 Agrawal, Y. C., E. A. Terray, and M. Donelan, 1992: Enhanced dissipation of kinetic energy
870 beneath surface waves. *Nature*, **359**, 219–220.
- 871 Anis, A. and J. N. Moum, 1995: Surface wave-turbulence interactions: Scaling $\epsilon(z)$ near the
872 sea surface. *J. Phys. Oceanogr.*, **25**, 2025–2045.
- 873 Ardhuin, F., B. Chapron, and F. Collard, 2009: Observation of swell dissipation across
874 oceans. *Geophysical Research Letters*, **36 (6)**, L06 607.
- 875 Ardhuin, F., et al., 2010: Semiempirical dissipation source functions for ocean waves. part
876 i: Definition, calibration, and validation. *J. Phys. Oceanogr.*, **40 (9)**, 1917–1941.
- 877 Babanin, A. V., 2011: *Breaking and Dissipation of Ocean Surface Waves*. Cambridge Univ.
878 Press, New York.
- 879 Babanin, A. V. and D. Chalikov, 2012: Numerical investigation of turbulence generation in
880 non-breaking potential waves. *J. Geophys. Res.*, **117 (C06010)**.
- 881 Babanin, A. V., D. Chalikov, I. R. Young, and I. Savelyev, 2010a: Numerical and laboratory
882 investigation of breaking of steep two-dimensional waves in deep water. *J. Fluid Mech.*,
883 **644**, 433–463.
- 884 Babanin, A. V. and B. K. Haus, 2009: On the existence of water turbulence induced by
885 non-breaking surface waves. *J. Phys. Oceanogr.*, **39**, 2675–2679.
- 886 Babanin, A. V., K. N. Tsagareli, I. R. Young, and D. J. Walker, 2010b: Numerical investiga-
887 tion of spectral evolution of wind waves. part 2. dissipation function and evolution tests.
888 *J. Phys. Oceanogr.*, **40 (4)**, 667–683.

- 889 Banner, M. L., A. V. Babanin, and I. Young, 2000: Breaking probability for dominant waves
890 on the sea surface. *J. Phys. Oceanogr.*, **30**, 3145–3160.
- 891 Banner, M. L., J. R. Gemmrich, and D. Farmer, 2002: Multiscale measurements of ocean
892 wave breaking probability. *J. Phys. Oceanogr.*, **32**, 3364–3375.
- 893 Banner, M. L. and D. H. Peregrine, 1993: Wave breaking in deep water. *Annu. Rev. Fluid*
894 *Mech.*, **25**, 373–397.
- 895 Banner, M. L. and W. L. Pierson, 2007: Wave breaking onset and strength for two-
896 dimensional deep water wave groups. *J. Fluid Mech.*, **585**, 93–115.
- 897 CERC, 1977: *Shore protection manual*. U.S. Army Coastal Engineering Research Center, 3d
898 ed.
- 899 Chickadel, C. C., R. A. Holman, and M. H. Freilich, 2003: An optical technique for the
900 measurement of longshore currents. *Journal of Geophysical Research*, **108 (C11)**, 1–17.
- 901 Ding, L. and D. Farmer, 1994: Observations of breaking wave statistics. *J. Phys. Oceanogr.*,
902 **24**, 1368–1387.
- 903 Dobson, F., W. Perrie, and B. Toulany, 1989: On the deep-water fetch laws for wind-
904 generated surface gravity-waves. *Atmosphere-Ocean*, **27**, 210–236.
- 905 Donelan, M., J. Hamilton, and W. H. Hui, 1985: Directional spectra of wind-generated
906 waves. *Phil. Trans R. Soc. Lond. A*, **315 (1534)**, 509–562.
- 907 Donelan, M., M. Skafel, H. Graber, P. Liu, D. Schwab, and S. Venkatesh, 1992: On the
908 growth-rate of wind-generated waves. *Atmosphere-Ocean*, **30**, 457–478.
- 909 Drazen, D., W. K. Melville, and L. Lenain, 2008: Inertial scaling of dissipation in unsteady
910 breaking waves. *J. Fluid Mech.*, **611**, 307–332.

- 911 Duncan, J. H., 1981: An experimental investigation of breaking waves produced by a towed
912 hydrofoil. *Proc. R. Soc. London Ser. A*, **377**, 331–348.
- 913 Duncan, J. H., 1983: The breaking and non-breaking wave resistance of a two-dimensional
914 hydrofoil. *J. Fluid Mech.*, **126**, 507–520.
- 915 Duncan, J. H., 2001: Spilling breakers. *Annu. Rev. Fluid Mech.*, **33**, 519–547.
- 916 Gemmrich, J., 2010: Strong turbulence in the wave crest region. *J. Phys. Oceanogr.*, **40**,
917 583–595.
- 918 Gemmrich, J., T. Mudge, and V. Polonichko, 1994: On the energy input from wind to surface
919 waves. *J. Phys. Oceanogr.*, **24**, 2413–2417.
- 920 Gemmrich, J. R., M. L. Banner, and C. Garrett, 2008: Spectrally resolved energy dissipation
921 rate and momentum flux of breaking waves. *J. Phys. Oceanogr.*, **38**, 1296–1312.
- 922 Gemmrich, J. R. and D. Farmer, 1999: Observations of the scale and occurrence of breaking
923 surface waves. *J. Phys. Oceanogr.*, **29**, 2595–2606.
- 924 Gemmrich, J. R. and D. Farmer, 2004: Near-surface turbulence in the presence of breaking
925 waves. *J. Phys. Ocean.*, **34**, 1067–1086.
- 926 Hasselmann, K., et al., 1973: Measurements of wind-wave growth and swell decay during
927 the join north sea wave project. *Duet. Hydrogr. Z*, **8 (12)**, 1–95.
- 928 Herbers, T. H. C., P. F. Jessen, T. T. Janssen, D. B. Colbert, and J. H. MacMahan, 2012:
929 Observing ocean surface waves with gps-tracked buoys. *J. Atmos. Ocean. Tech.*, **29**, 944–
930 959.
- 931 Holland, K. T., R. A. Holman, T. C. Lippmann, J. Stanley, and N. Plant, 1997: Practical
932 use of video imagery in nearshore oceanographic field studies. *IEEE Journal of Oceanic*
933 *Engineering*, **22**, 81–92.

- 934 Janssen, P. A. E. M., 1991: Quasi-linear theory of wave generation applied to wave forecast-
935 ing. *J. Phys. Oceanogr.*, **21**, 1631–1642.
- 936 Jessup, A. and K. Phadnis, 2005: Measurement of the geometric and kinematic properties
937 of microscale breaking waves from infrared imagery using a PIV algorithm. *Measur. Sci.*
938 *Tech.*, **16**, 1961–1969.
- 939 Jessup, A., C. Zappa, and M. Loewen, 1997: Infrared remote sensing of breaking waves.
940 *Nature*, **385**, 52–55.
- 941 Kitaigorodskii, S., 1962: Contribution to an analysis of the spectra of wind-caused wave
942 action. *Izv. Akad. Nauk SSSR Geophys.*, **9**, 1221–1228.
- 943 Kitaigorodskii, S., M. Donelan, J. L. Lumley, and E. A. Terray, 1983: Wave turbulence
944 interactions in the upper ocean. part ii. statistical characteristics of wave and turbulent
945 components of the random velocity field in the marine surface layer. *J. Phys. Oceanogr.*,
946 **13**, 1988–1999.
- 947 Kleiss, J. M. and W. K. Melville, 2010: Observations of wave breaking kinematics in fetch-
948 limited seas. *J. Phys. Ocean.*, **40**, 2575–2604.
- 949 Kleiss, J. M. and W. K. Melville, 2011: The analysis of sea surface imagery for whitecap
950 kinematics. *J. Atmos. Ocean. Tech.*, **28**, 219–243.
- 951 Large, W. and S. Pond, 1981: Open ocean momentum flux measurements in moderate to
952 strong winds. *J. Phys. Oceanogr.*, **11**, 324–336.
- 953 Loewen, M. R. and W. K. Melville, 1991: Microwave backscatter and acoustic radiation from
954 breaking waves. *J. Fluid Mech.*, **224**, 601–623.
- 955 Melville, W. K., 1994: Energy dissipation by breaking waves. *J. Phys. Oceanogr.*, **24**, 2041–
956 2049.

- 957 Melville, W. K., 1996: The role of surface-wave breaking in air-sea interaction. *Annu. Rev.*
958 *Fluid Mech.*, **28**, 279–321.
- 959 Melville, W. K. and P. Matusov, 2002: Distribution of breaking waves at the ocean surface.
960 *Nature*, **417**, 58–63.
- 961 Phillips, O. M., 1958: The equilibrium range in the spectrum of wind-generated ocean waves.
962 *J. Fluid Mech.*, **4**, 426–434.
- 963 Phillips, O. M., 1985: Spectral and statistical properties of the equilibrium range in wind-
964 generated gravity waves. *J. Fluid Mech.*, **156**, 495–531.
- 965 Phillips, O. M., F. Posner, and J. Hansen, 2001: High range resolution radar measurements of
966 the speed distribution of breaking events in wind-generated ocean waves: Surface impulse
967 and wave energy dissipation rates. *J. Phys. Ocean.*, **31**, 450–460.
- 968 Plant, W. J., 2012: Whitecaps in deep water. *Geophys. Res. Lett.*, **39** (L16601).
- 969 Rapp, R. J. and W. K. Melville, 1990: Laboratory measurements of deep-water breaking
970 waves. *Phil. Trans R. Soc. Lond. A*, **331**, 735–800.
- 971 Rogers, W. E., A. V. Babanin, and D. W. Wang, 2012: Observation-consistent input and
972 whitecapping dissipation in a model for wind-generated surface waves: description and
973 simple calculations. *J. Atmos. Ocean. Tech.*, **29**, 1329–1346.
- 974 Romero, L. and W. K. Melville, 2010: Airborne observations of fetch-limited waves in the
975 gulf of Tehuantepec. *J. Phys. Ocean.*, **40**, 441–465.
- 976 Romero, L., W. K. Melville, and J. M. Kleiss, 2012: Spectral energy dissipation due to
977 surface-wave breaking. *J. Phys. Oceanogr.*, **42**, 1421–1444.
- 978 Smith, P. C. and J. I. Macpherson, 1987: Cross-shore variations of near-surface wind velocity
979 and atmospheric-turbulence at the land-sea boundary during casp. *Atmosphere-Ocean*,
980 **25** (3), 279–303.

- 981 Stansell, P. and C. MacFarlane, 2002: Experimental investigation of wave breaking criteria
982 based on wave phase speeds. *J. Phys. Oceanogr.*, **32**, 1269–1283.
- 983 Sutherland, P. and W. K. Melville, 2013: Field measurements and scaling of ocean surface
984 wave-breaking statistics. *Geophys. Res. Let.*, **40**, 3074–3079.
- 985 Terray, E., M. Donelan, Y. Agrawal, W. Drennan, K. Kahma, A. Williams, P. Hwang, and
986 S. Kitaigorodskii, 1996: Estimates of kinetic energy dissipation under breaking waves. *J.*
987 *Phys. Oceanogr.*, **26**, 792–807.
- 988 Thomson, J., 2012: Wave breaking dissipation observed with 'swift' drifters. *J. Atmos.*
989 *Ocean. Tech.*, **29 (12)**, 1866–1882.
- 990 Thomson, J. and A. Jessup, 2009: A fourier-based method for the distribution of breaking
991 crests from video observations. *J. Atmos. Ocean. Tech.*, **26**, 1663–1671.
- 992 Thomson, J., A. Jessup, and J. Gemmrich, 2009: Energy dissipation and the spectral distri-
993 bution of whitecaps. *Geophys. Res. Let.*, **36 (L11601)**.
- 994 Thorpe, S., 1995: Dynamical processes of transfer at the sea surface. *Prog. Oceanog.*, **35**,
995 315–352.
- 996 Toba, Y., 1973: Local balance in the air-sea boundary process, iii. on the spectrum of wind
997 waves. *J. Oceanogr. Soc. Japan*, **29**, 209–220.
- 998 Wiles, P., T. P. Rippeth, J. Simpson, and P. Hendricks, 2006: A novel technique for measur-
999 ing the rate of turbulent dissipation in the marine environment. *Geophys. Res. Let.*, **33**,
1000 L21 608.
- 1001 Yelland, M., P. Taylor, I. Consterdine, and M. Smith, 1994: The use of the inertial dissipation
1002 technique for shipboard wind stress determination. *J. Atmos. Ocean. Tech.*, **11**, 1093–1108.
- 1003 Young, I., 1999: *Wind Generated Ocean Waves*. Elsevier Ocean Engineering Book Series,
1004 Elsevier, New York.

1005 Young, I. R. and A. V. Babanin, 2006: Spectral distribution of energy dissipation of wind-
1006 generated waves due to dominant wave breaking. *J. Phys. Oceanogr.*, **36**, 376–394.

1007 List of Tables

- 1008 1 Date, time, fetch, and duration of the 9 $\Lambda(c)$ observations. Also shown are
1009 the bulk wave and wind quantities, calculated as 500-meter averages around
1010 each point in fetch. 45
- 1011 2 Linear fits of the daily wave energy growth with fetch, for SWIFTs 1 and
1012 2. When multiplied by c_g , $\overline{\partial E / \partial x}$ gives an estimate of the advective wave
1013 growth. The intercept indicates the value of fetch for which the linear fit
1014 extrapolates to give zero wave energy. R^2 values and 95% confidence intervals
1015 (in W s m^{-3}) are also shown. 46
- 1016 3 Linear fits of the daily wave energy growth with time, for SWIFTs 1 and 2.
1017 For each day, $\overline{\partial E / \partial t}$ gives an estimate of the temporal wave growth. R^2 values
1018 and 95% confidence intervals (in W m^{-2}) are also shown. 47

TABLE 1. Date, time, fetch, and duration of the 9 $\Lambda(c)$ observations. Also shown are the bulk wave and wind quantities, calculated as 500-meter averages around each point in fetch.

| Date/Time | Duration [min] | Fetch [km] | H_s [m] | T_e [s] | U_{10} [m s ⁻¹] | u_* [m s ⁻¹] |
|-----------------------|----------------|------------|-----------|-----------|-------------------------------|----------------------------|
| 19:10 UTC 14 Feb 2011 | 6.8 | 1.40 | 0.56 | 2.55 | 9.74 | 0.45 |
| 20:36 UTC 14 Feb 2011 | 6.5 | 3.01 | 0.71 | 2.61 | 11.50 | 0.37 |
| 20:48 UTC 14 Feb 2011 | 5.1 | 3.37 | 0.76 | 2.64 | 12.55 | 0.42 |
| 21:34 UTC 14 Feb 2011 | 6.5 | 5.24 | 1.08 | 2.89 | 15.07 | 0.56 |
| 21:41 UTC 14 Feb 2011 | 8.5 | 5.60 | 1.12 | 2.97 | 15.73 | 0.60 |
| 22:27 UTC 14 Feb 2011 | 6.0 | 8.33 | 1.26 | 3.11 | 17.24 | 0.64 |
| 22:35 UTC 14 Feb 2011 | 4.8 | 8.84 | 1.29 | 3.14 | 18.01 | 0.66 |
| 19:04 UTC 15 Feb 2011 | 10.0 | 12.55 | 0.86 | 2.87 | 11.45 | 0.36 |
| 19:27 UTC 15 Feb 2011 | 6.0 | 13.17 | 1.00 | 2.97 | 13.11 | 0.48 |

TABLE 2. Linear fits of the daily wave energy growth with fetch, for SWIFTs 1 and 2. When multiplied by c_g , $\overline{\partial E/\partial x}$ gives an estimate of the advective wave growth. The intercept indicates the value of fetch for which the linear fit extrapolates to give zero wave energy. R^2 values and 95% confidence intervals (in W s m^{-3}) are also shown.

| Day | SWIFT | $\overline{\partial E/\partial x}$ [W s m^{-3}] | Intercept [km] | R^2 | 95% CI |
|---------|-------|--|----------------|-------|---------------------------|
| Feb. 14 | 1 | 0.125 | -0.23 | 0.951 | $\pm 1.51 \times 10^{-2}$ |
| Feb. 14 | 2 | 0.111 | -0.41 | 0.931 | $\pm 1.60 \times 10^{-2}$ |
| Feb. 15 | 1 | 0.152 | 9.46 | 0.926 | $\pm 4.95 \times 10^{-2}$ |
| Feb. 15 | 2 | 0.230 | 11.97 | 0.852 | $\pm 1.33 \times 10^{-1}$ |

TABLE 3. Linear fits of the daily wave energy growth with time, for SWIFTs 1 and 2. For each day, $\overline{\partial E/\partial t}$ gives an estimate of the temporal wave growth. R^2 values and 95% confidence intervals (in W m^{-2}) are also shown.

| Day | SWIFT | $\overline{\partial E/\partial t}$ [W m^{-2}] | R^2 | 95% CI |
|---------|-------|--|-------|---------------------------|
| Feb. 14 | 1 | 0.075 | 0.915 | $\pm 1.21 \times 10^{-2}$ |
| Feb. 14 | 2 | 0.067 | 0.873 | $\pm 1.35 \times 10^{-2}$ |
| Feb. 15 | 1 | 0.065 | 0.955 | $\pm 1.63 \times 10^{-2}$ |
| Feb. 15 | 2 | 0.093 | 0.816 | $\pm 6.13 \times 10^{-2}$ |

1019 List of Figures

- 1020 1 Summary of conditions during the two days of observations. (b) Map of the
1021 Pacific Northwest showing the Strait of Juan de Fuca. The red box corre-
1022 sponds to the edges of (a), which shows instrument and ship tracks during
1023 February 14 and 15. The dashed line is the zero-fetch line. The solid lines are
1024 the tracks of the *R/V Robertson* and Dopbeam (black), SWIFT 1 (red), and
1025 SWIFT 2 (cyan). The yellow arrow shows the average direction of the wind
1026 from both days. (c-f) Evolution of the wave and wind conditions with fetch
1027 measured from SWIFT 1 (red), SWIFT 2 (cyan), and the *R/V Robertson*
1028 (black line in wind measurements). Conditions shown are (c) significant wave
1029 height, (d) peak energy period, (e) 10-meter wind speed, (f) friction velocity,
1030 and (g) wave age. 52
- 1031 2 Wave frequency spectra colored by fetch (a) and u_* (b). Also shown are power
1032 laws of the form f^{-4} and f^{-5} . 53
- 1033 3 (a) Turbulent dissipation profiles from SWIFT 1 plotted with fetch. Depth,
1034 z , is measured from the instantaneous sea surface. (b) Total (integrated)
1035 turbulent dissipation measured by SWIFT 1 (red), SWIFT 2 (cyan), and
1036 Dopbeam system (blue) vs. fetch, averaged over 500 meters. The background
1037 dissipation level of 0.5 W m^{-2} has not been subtracted from these values, but
1038 is shown as the lower axis limit of panel (b). 54
- 1039 4 Sample images of breaking from shipboard and SWIFT video. Images (a, b,
1040 c) are taken from February 14, 19:13 UTC, during calmer wave conditions.
1041 Images (d, e, f) are taken from February 15, 19:27 UTC, during steeper wave
1042 conditions. (a) and (d) are raw, stabilized shipboard images, with the red
1043 box showing the sampled field of view. (b) and (e) are the corresponding
1044 thresholded, binary images in rectified real-world coordinates. (c) and (f) are
1045 sample SWIFT images from coincident times. 55

- 1046 5 $\Lambda(c)$ vs dimensional (a,c) and non-dimensional (b,d) phase speed, in linear
1047 (a,b) and logarithmic (c,d) coordinates. All curves colored by mean square
1048 slope. Dashed curves are $\Lambda(c)$ results shown to be biased low by comparison
1049 with SWIFT breaking rate estimates. Black dashed line is the c^{-6} power law
1050 derived in Phillips (1985). 56
- 1051 6 Time series of (a) wind speed, (b) wind direction, and (c) wave height from
1052 nearby NDBC stations: the Smith Island Meteorological C-MAN Station
1053 (#SISW1, magenta) and the New Dungeness 3-meter discus buoy (#46088,
1054 green). Black points are experimental values measured from the *R/V Robert-*
1055 *son* (a,b) and the SWIFTs (c). 57
- 1056 7 Evolution of four wave parameters plotted against non-dimensional fetch. (a)
1057 Non-dimensional wave energy. Black circles use the mean daily wind speed,
1058 blue triangles use a linear fetch-integrated wind speed, and red crosses use the
1059 instantaneous wind speed. Green symbols show the values from the NDBC
1060 #46088 wave buoy, taken from the shaded areas on Figure 6, with error bars
1061 for the minimum and maximum of the range of values. The Young (1999) em-
1062 pirical relation is shown by the black dashed line with gray range of parameters
1063 and fully-developed limits (horizontal solid black line). (b) Non-dimensional
1064 frequency, symbols as in (a). (c) Mean square slope. (d) Drag coefficient 58
- 1065 8 Evaluation and comparison of wave fluxes. Gray shaded regions show possible
1066 range of wind input (a), wave energy flux (b), and breaking dissipation (c) vs.
1067 fetch. Black lines come from a stationary assumption, $\partial E/\partial t = 0$, and using
1068 the mean value of $c_{eff} = 0.5$. Colored curves of dissipation are calculated
1069 directly from turbulent dissipation for SWIFT 1 (red), SWIFT 2 (cyan), and
1070 Dopbeam (blue), with a background dissipation level of 0.5 W m^{-2} subtracted
1071 off. All quantities are 500-meter averages. 59

- 1072 9 (a) Breaking rate and (b) wave dissipation vs. mean square slope. (a) Circles
1073 correspond to shipboard measurements from February 14 and squares are from
1074 shipboard measurements during February 15. Asterisks and crosses are from
1075 manual SWIFT breaking rate counts for February 14 and 15, respectively.
1076 Data plotted with open symbols overlap with the SWIFT breaking rates (in
1077 time) and appear to underestimate the breaking rate. (b) Wave dissipation
1078 from Figure 8 plotted vs. mean square slope, for SWIFT 1 (red), SWIFT 2
1079 (cyan), Dopbeam (blue), and inferred dissipation from the RTE based on the
1080 stationary assumption (black). 60
- 1081 10 Breaking strength parameter, b , plotted against mean square slope (a), inverse
1082 wave age (b), and peak steepness (c). Coloring as in Figure 9b and symbols
1083 from Figure 9a. Open symbols are used for data with known bias. Additional
1084 data from Lake Washington in 2006 (green crosses) and Puget Sound in 2008
1085 (magenta crosses) described in Thomson et al. (2009). Vertical bars to the
1086 right of the plots show ranges of b estimates from Thomson et al. (2009)
1087 (green), Gemmrich et al. (2008) (magenta), Phillips et al. (2001) (light blue),
1088 and Banner and Pierson (2007) (dark red). For Drazen et al. (2008) (dark
1089 blue), the expected b for these steepness is extrapolated from their power law
1090 fit. For Romero et al. (2012) (orange), the range of b for $c \leq c_p$ is shown. 61
- 1091 11 Sensitivities and error bars for the b data with the SWIFT S_{ds} values. Error
1092 bars come from (a) ± 1 standard deviation in the values of b from 50 runs
1093 of synthetic data, (b) estimated error in the SWIFT dissipation values, (c)
1094 varying the threshold value in converting differenced images to binary by
1095 $\pm 20\%$, (d) varying the upper limit of integration of $c^5 \Lambda(c) dc$ (originally c_p) by
1096 $\pm 20\%$, and (e) varying α in $c = \alpha c_{brk}$ by $0.7 \leq \alpha \leq 1$. Gray points indicate b
1097 values which are biased by small-scale breaking. 62

- 1098 12 Comparison of the true $\Lambda(c)$ distribution (solid black) with the estimate from
1099 the Fourier method for 50 runs of synthetic data (gray), with inputs similar
1100 to the $\Lambda(c)$ data from February 14, 21:34 UTC. 63
- 1101 13 (a) Wave height spectra vs. normalized phase speed, c/c_p . All lines colored
1102 by mean square slope. Shading divides the spectra into peak and equilibrium
1103 (and possibly saturation) ranges, using a cut-off of $0.7c_p$. (b) $\Lambda(c)$ from Figure
1104 5. (c) $b_1(c)$ model from Romero et al. (2012) using the azimuthal-integrated
1105 saturation spectra, σ , and coefficients $A_1 = 4.5$ and $B_T = 9.3 \times 10^{-4}$. 64
- 1106 14 Comparison of $\Lambda(c)$ results from the Fourier method with synthetic data input
1107 in linear (a) and logarithmic (b) coordinates. The “true” distribution (dotted)
1108 is the Gaussian input distribution for the synthetic data. Speeds and ampli-
1109 tudes are relative to the peak in the true distribution. The “original” Fourier
1110 method curve (dashed) uses the wavenumber-specific signal-to-noise filtering
1111 of Thomson and Jessup (2009). The “modified” Fourier method (solid) uses
1112 a constant signal-to-noise cut-off throughout the spectrum. 65
- 1113 15 (a) Comparison of mean crest width in pixels with crest advancement speed in
1114 pixels for both February 14 (circles) and February 15 (squares). (b) Compar-
1115 ison of calculated breaking rate from the first moment of $\Lambda(c)$, R_Λ , with the
1116 direct breaking rate R_I for the original distribution. R_Λ are shown without
1117 width correction (“original,” x’s for February 14, crosses for February 15),
1118 and with width correction (“corrected,” circles for February 14, squares for
1119 February 15). 66

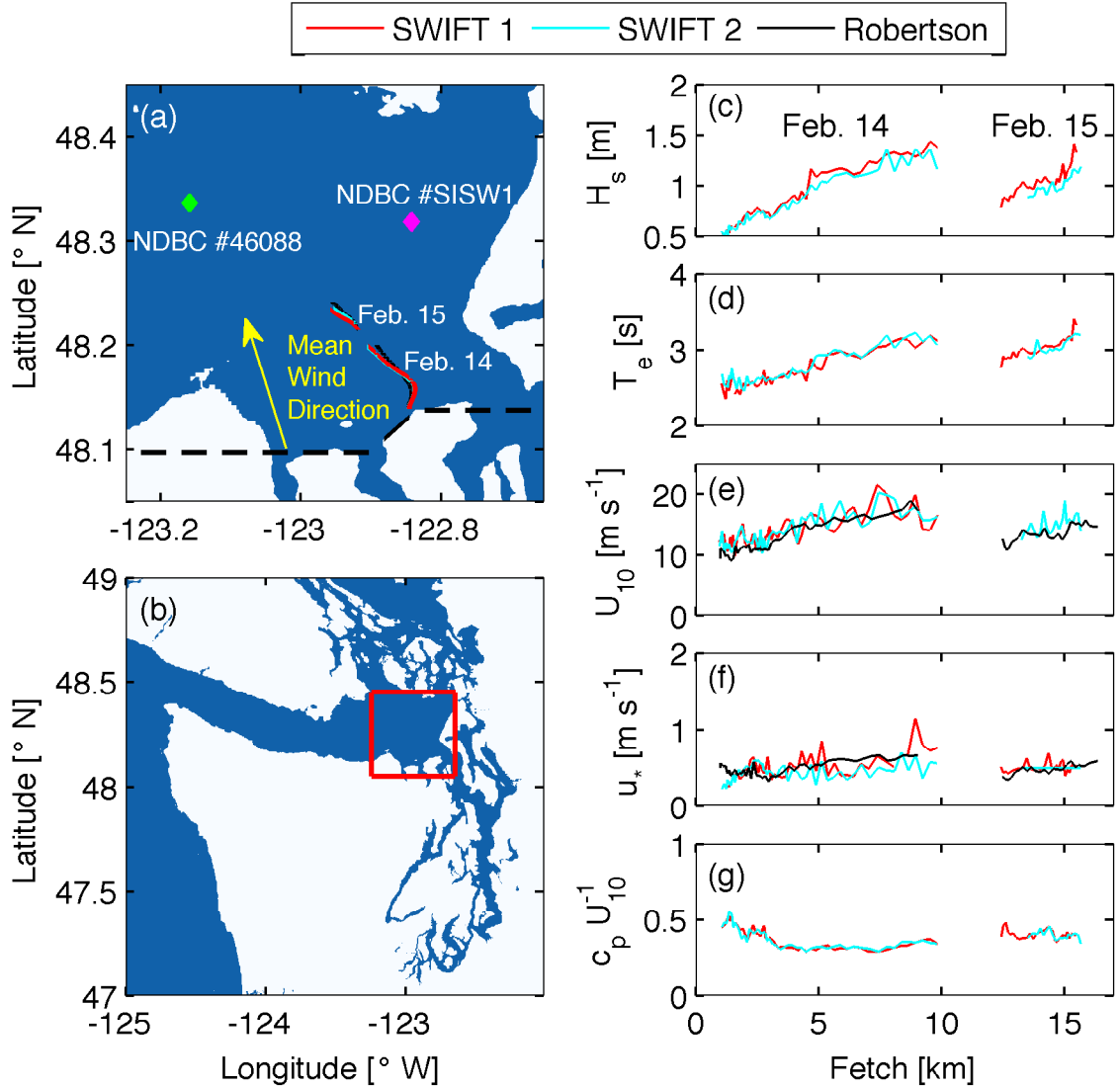


FIG. 1. Summary of conditions during the two days of observations. (b) Map of the Pacific Northwest showing the Strait of Juan de Fuca. The red box corresponds to the edges of (a), which shows instrument and ship tracks during February 14 and 15. The dashed line is the zero-fetch line. The solid lines are the tracks of the *R/V Robertson* and *Dopbeam* (black), SWIFT 1 (red), and SWIFT 2 (cyan). The yellow arrow shows the average direction of the wind from both days. (c-f) Evolution of the wave and wind conditions with fetch measured from SWIFT 1 (red), SWIFT 2 (cyan), and the *R/V Robertson* (black line in wind measurements). Conditions shown are (c) significant wave height, (d) peak energy period, (e) 10-meter wind speed, (f) friction velocity, and (g) wave age.

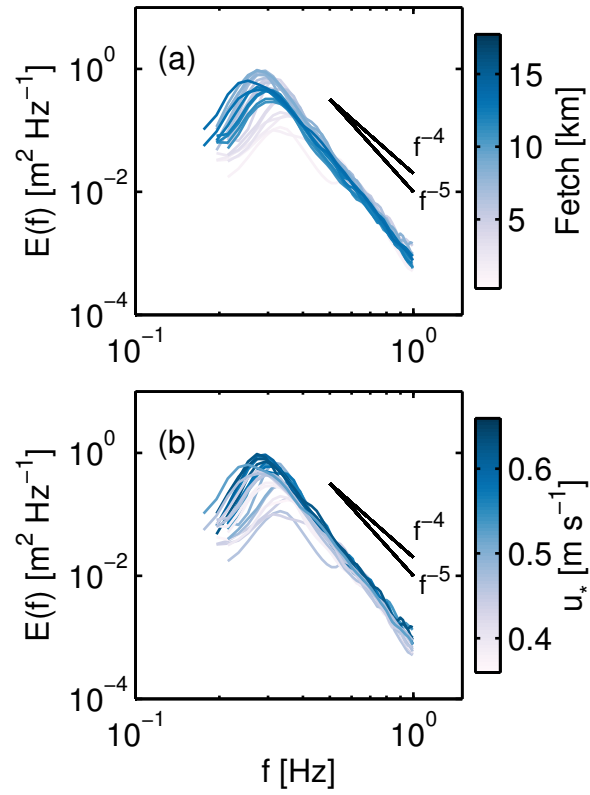


FIG. 2. Wave frequency spectra colored by fetch (a) and u_* (b). Also shown are power laws of the form f^{-4} and f^{-5} .

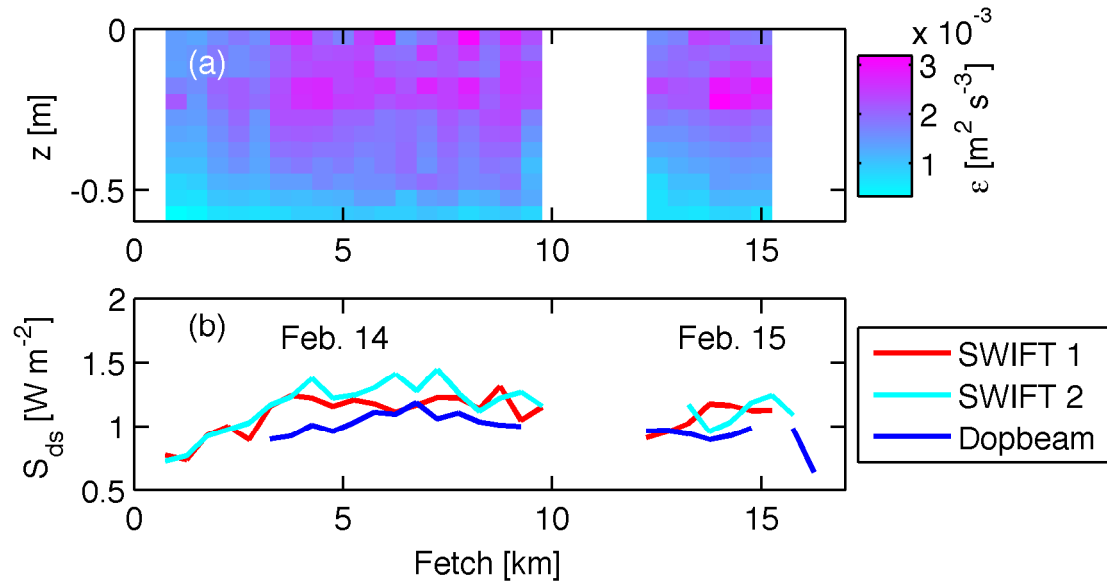


FIG. 3. (a) Turbulent dissipation profiles from SWIFT 1 plotted with fetch. Depth, z , is measured from the instantaneous sea surface. (b) Total (integrated) turbulent dissipation measured by SWIFT 1 (red), SWIFT 2 (cyan), and Dopbeam system (blue) vs. fetch, averaged over 500 meters. The background dissipation level of 0.5 W m^{-2} has not been subtracted from these values, but is shown as the lower axis limit of panel (b).

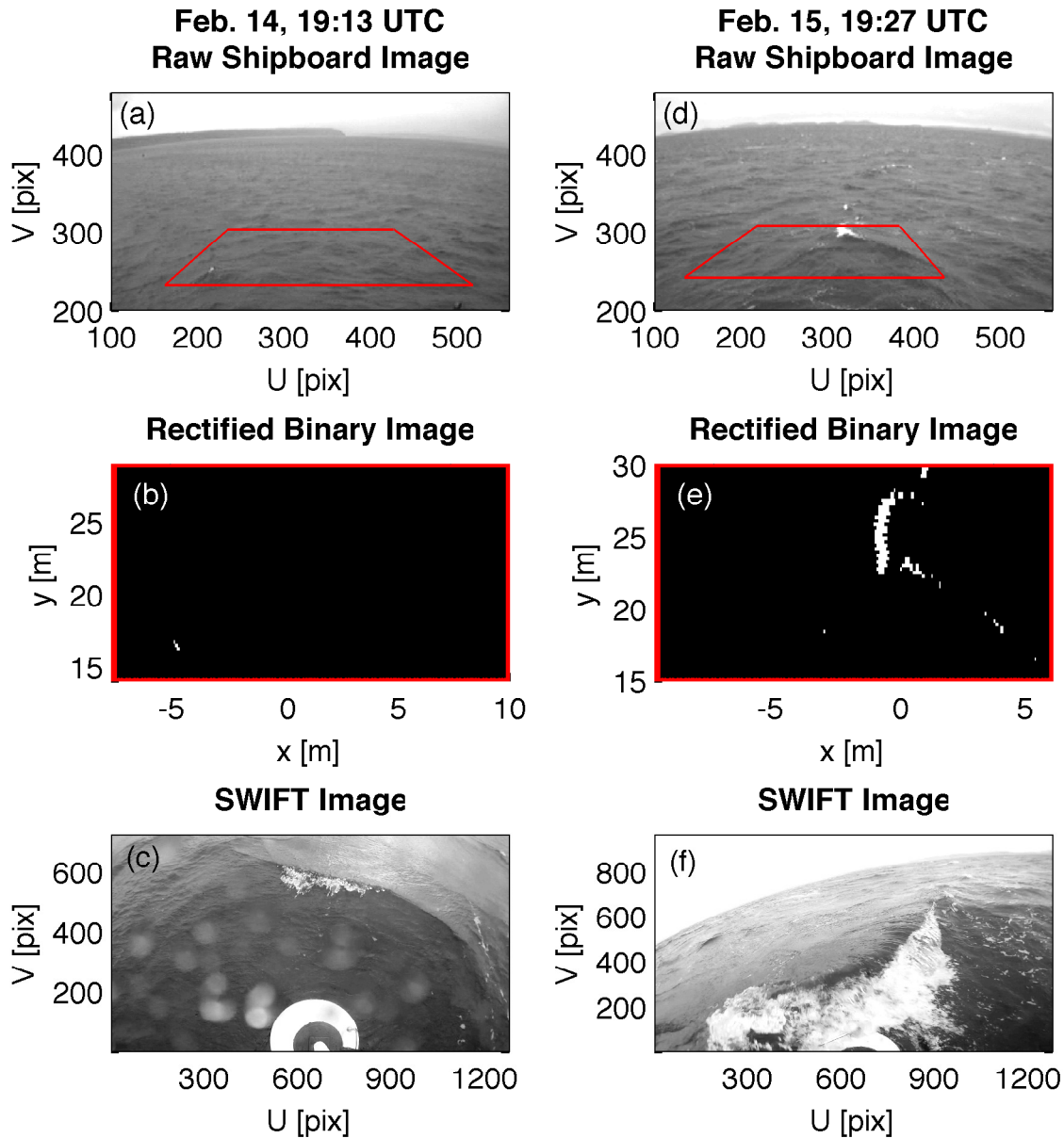


FIG. 4. Sample images of breaking from shipboard and SWIFT video. Images (a, b, c) are taken from February 14, 19:13 UTC, during calmer wave conditions. Images (d, e, f) are taken from February 15, 19:27 UTC, during steeper wave conditions. (a) and (d) are raw, stabilized shipboard images, with the red box showing the sampled field of view. (b) and (e) are the corresponding thresholded, binary images in rectified real-world coordinates. (c) and (f) are sample SWIFT images from coincident times.

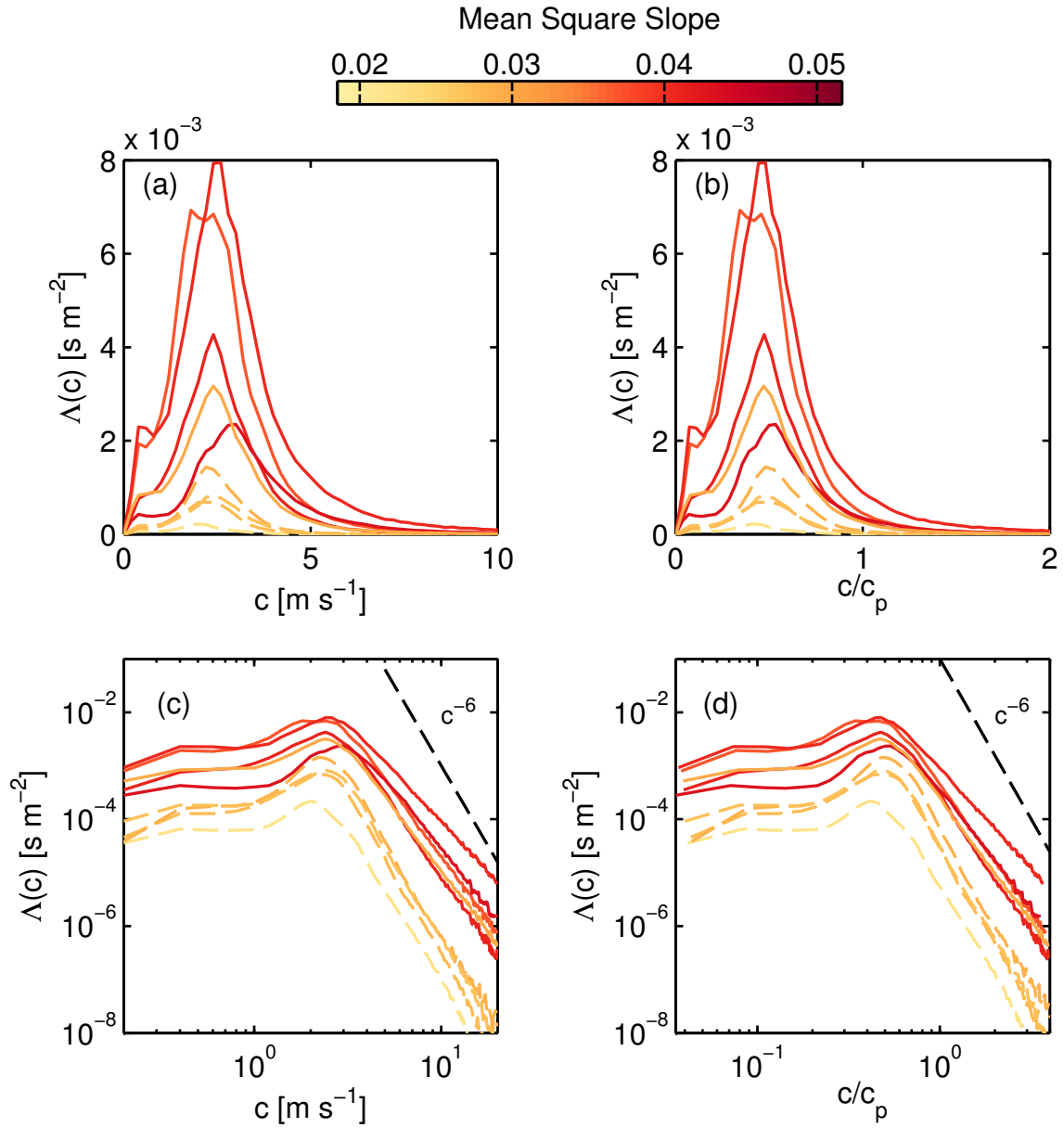


FIG. 5. $\Lambda(c)$ vs dimensional (a,c) and non-dimensional (b,d) phase speed, in linear (a,b) and logarithmic (c,d) coordinates. All curves colored by mean square slope. Dashed curves are $\Lambda(c)$ results shown to be biased low by comparison with SWIFT breaking rate estimates. Black dashed line is the c^{-6} power law derived in Phillips (1985).

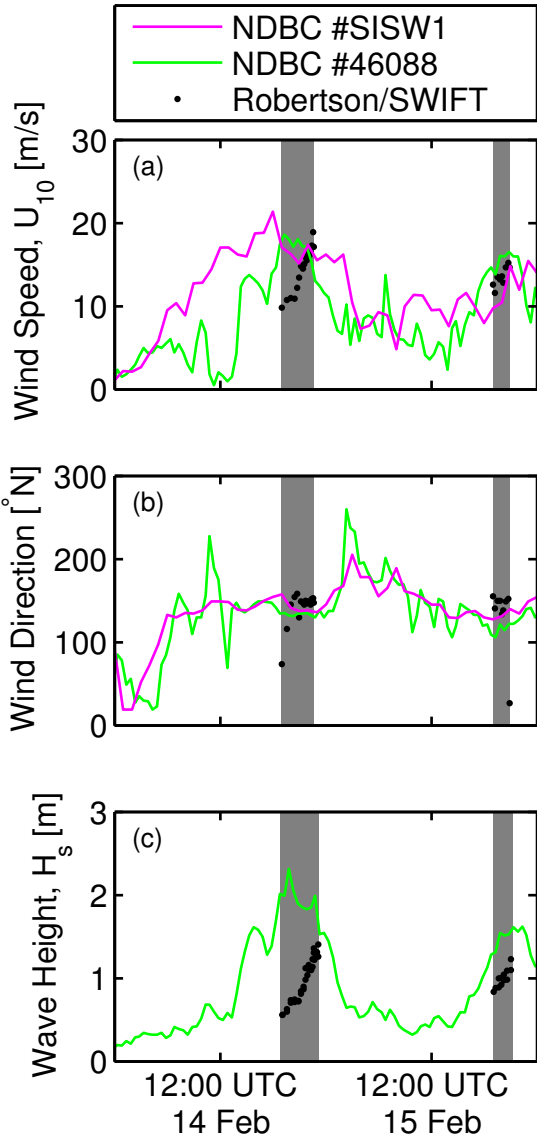


FIG. 6. Time series of (a) wind speed, (b) wind direction, and (c) wave height from nearby NDBC stations: the Smith Island Meteorological C-MAN Station (#SISW1, magenta) and the New Dungeness 3-meter discus buoy (#46088, green). Black points are experimental values measured from the *R/V Robertson* (a,b) and the SWIFTs (c).

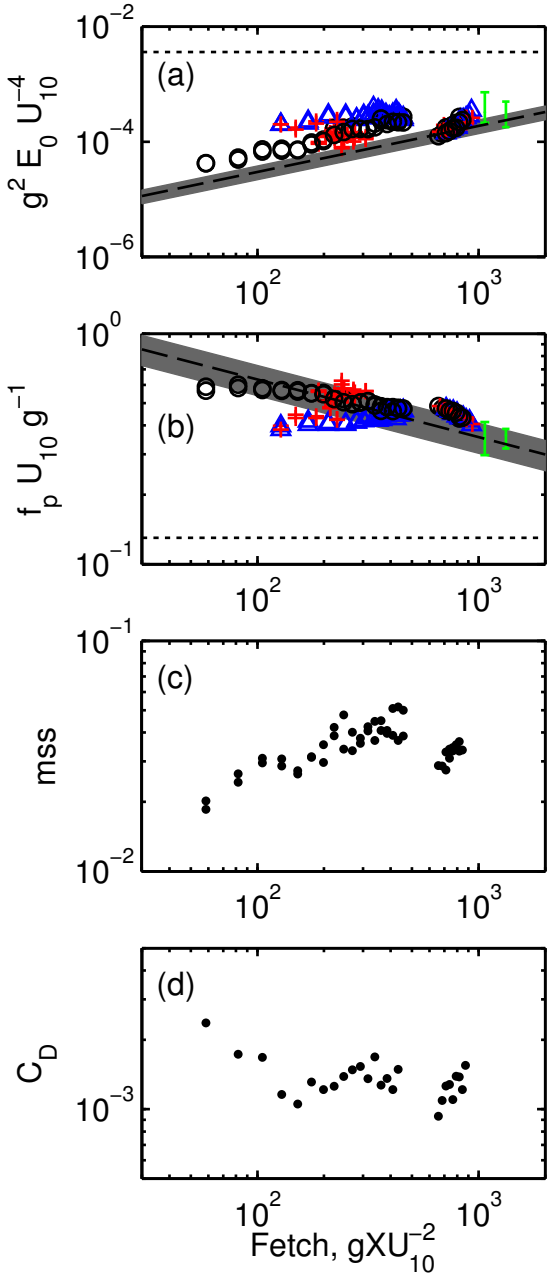


FIG. 7. Evolution of four wave parameters plotted against non-dimensional fetch. (a) Non-dimensional wave energy. Black circles use the mean daily wind speed, blue triangles use a linear fetch-integrated wind speed, and red crosses use the instantaneous wind speed. Green symbols show the values from the NDBC #46088 wave buoy, taken from the shaded areas on Figure 6, with error bars for the minimum and maximum of the range of values. The Young (1999) empirical relation is shown by the black dashed line with gray range of parameters and fully-developed limits (horizontal solid black line). (b) Non-dimensional frequency, symbols as in (a). (c) Mean square slope. (d) Drag coefficient

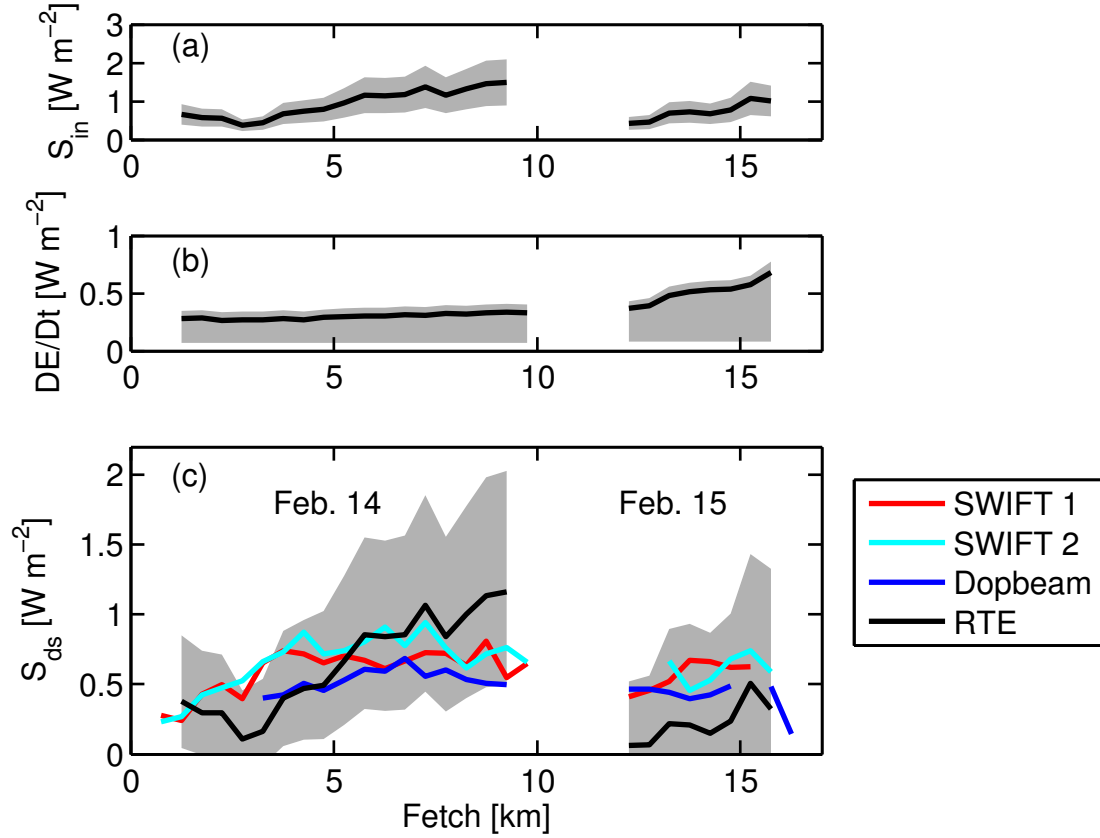


FIG. 8. Evaluation and comparison of wave fluxes. Gray shaded regions show possible range of wind input (a), wave energy flux (b), and breaking dissipation (c) vs. fetch. Black lines come from a stationary assumption, $\partial E/\partial t = 0$, and using the mean value of $c_{eff} = 0.5$. Colored curves of dissipation are calculated directly from turbulent dissipation for SWIFT 1 (red), SWIFT 2 (cyan), and Dopbeam (blue), with a background dissipation level of 0.5 W m^{-2} subtracted off. All quantities are 500-meter averages.

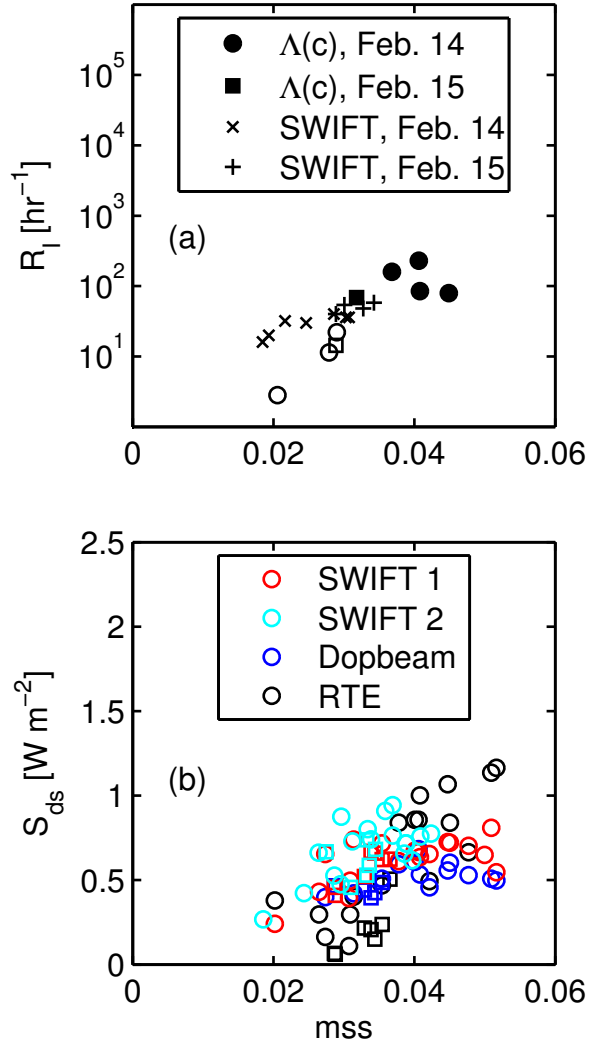


FIG. 9. (a) Breaking rate and (b) wave dissipation vs. mean square slope. (a) Circles correspond to shipboard measurements from February 14 and squares are from shipboard measurements during February 15. Asterisks and crosses are from manual SWIFT breaking rate counts for February 14 and 15, respectively. Data plotted with open symbols overlap with the SWIFT breaking rates (in time) and appear to underestimate the breaking rate. (b) Wave dissipation from Figure 8 plotted vs. mean square slope, for SWIFT 1 (red), SWIFT 2 (cyan), Dopbeam (blue), and inferred dissipation from the RTE based on the stationary assumption (black).

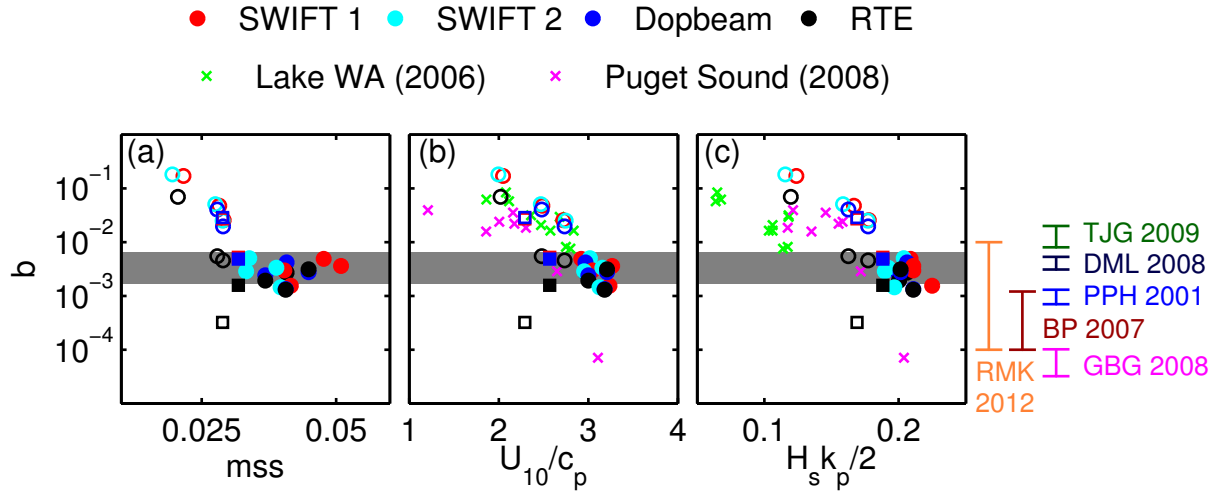


FIG. 10. Breaking strength parameter, b , plotted against mean square slope (a), inverse wave age (b), and peak steepness (c). Coloring as in Figure 9b and symbols from Figure 9a. Open symbols are used for data with known bias. Additional data from Lake Washington in 2006 (green crosses) and Puget Sound in 2008 (magenta crosses) described in Thomson et al. (2009). Vertical bars to the right of the plots show ranges of b estimates from Thomson et al. (2009) (green), Gemmrich et al. (2008) (magenta), Phillips et al. (2001) (light blue), and Banner and Pierson (2007) (dark red). For Drazen et al. (2008) (dark blue), the expected b for these steepness is extrapolated from their power law fit. For Romero et al. (2012) (orange), the range of b for $c \leq c_p$ is shown.

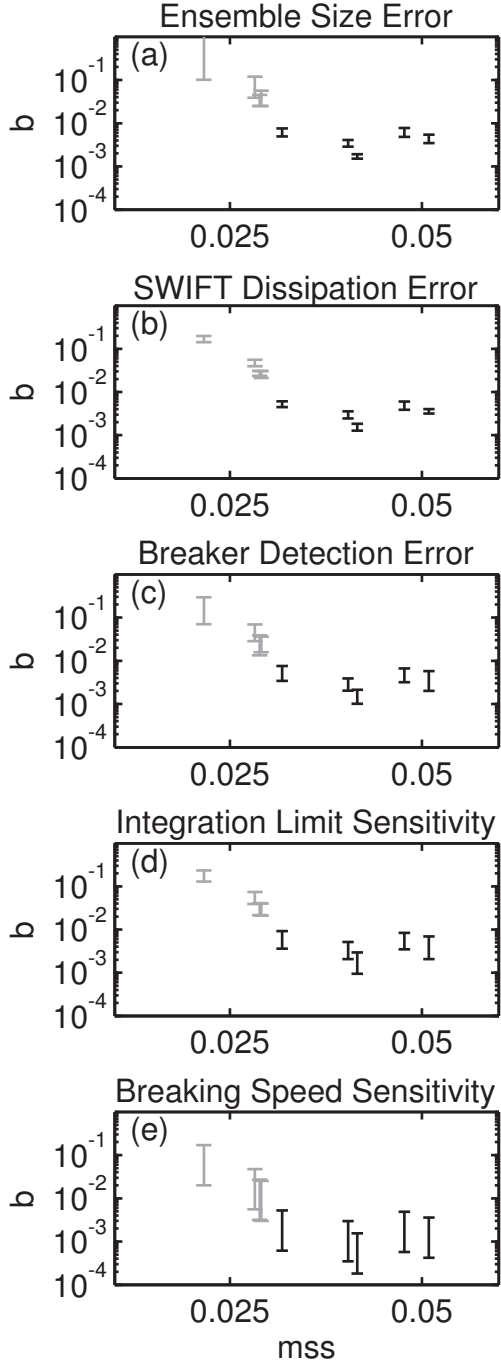


FIG. 11. Sensitivities and error bars for the b data with the SWIFT S_{ds} values. Error bars come from (a) ± 1 standard deviation in the values of b from 50 runs of synthetic data, (b) estimated error in the SWIFT dissipation values, (c) varying the threshold value in converting differenced images to binary by $\pm 20\%$, (d) varying the upper limit of integration of $c^5 \Lambda(c) dc$ (originally c_p) by $\pm 20\%$, and (e) varying α in $c = \alpha c_{brk}$ by $0.7 \leq \alpha \leq 1$. Gray points indicate b values which are biased by small-scale breaking.

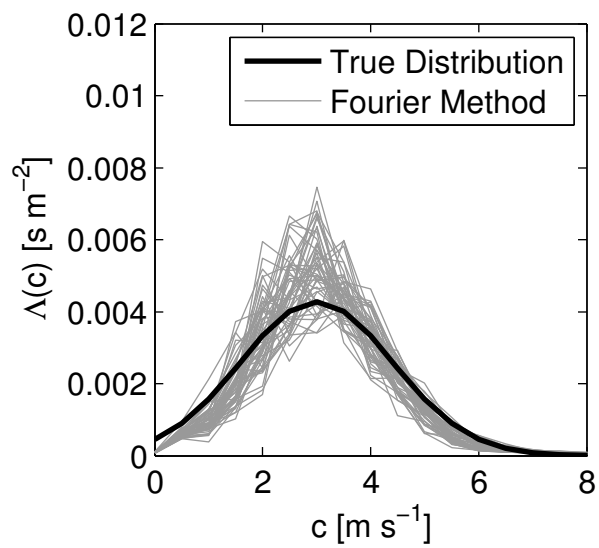


FIG. 12. Comparison of the true $\Lambda(c)$ distribution (solid black) with the estimate from the Fourier method for 50 runs of synthetic data (gray), with inputs similar to the $\Lambda(c)$ data from February 14, 21:34 UTC.

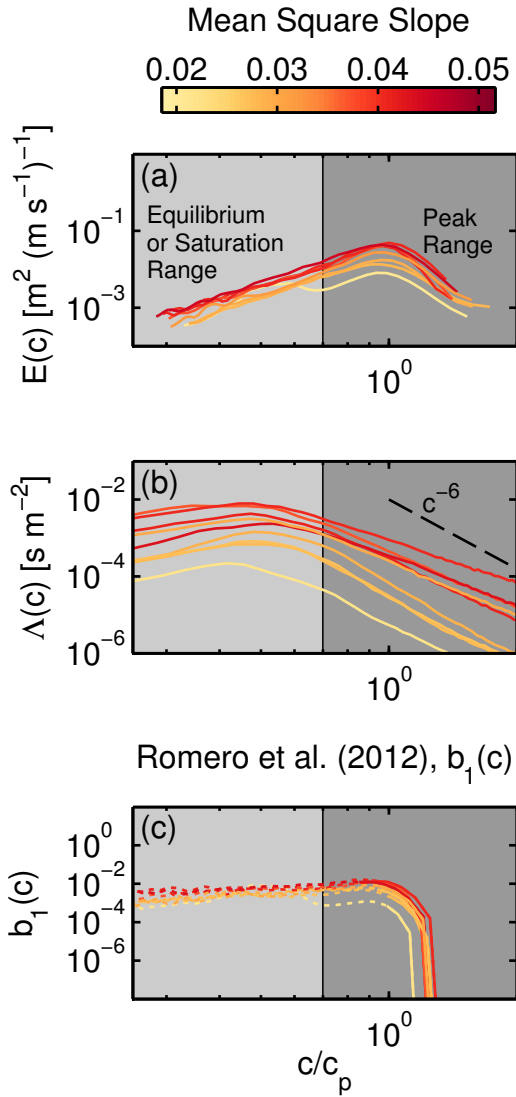


FIG. 13. (a) Wave height spectra vs. normalized phase speed, c/c_p . All lines colored by mean square slope. Shading divides the spectra into peak and equilibrium (and possibly saturation) ranges, using a cut-off of $0.7c_p$. (b) $\Lambda(c)$ from Figure 5. (c) $b_1(c)$ model from Romero et al. (2012) using the azimuthal-integrated saturation spectra, σ , and coefficients $A_1 = 4.5$ and $B_T = 9.3 \times 10^{-4}$.

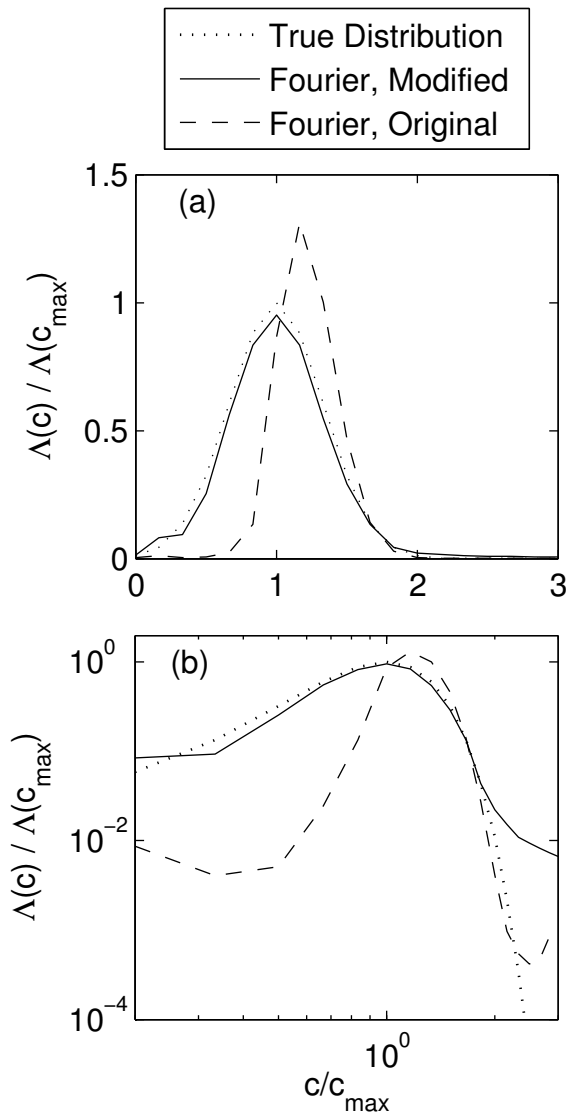


FIG. 14. Comparison of $\Lambda(c)$ results from the Fourier method with synthetic data input in linear (a) and logarithmic (b) coordinates. The “true” distribution (dotted) is the Gaussian input distribution for the synthetic data. Speeds and amplitudes are relative to the peak in the true distribution. The “original” Fourier method curve (dashed) uses the wavenumber-specific signal-to-noise filtering of Thomson and Jessup (2009). The “modified” Fourier method (solid) uses a constant signal-to-noise cut-off throughout the spectrum.

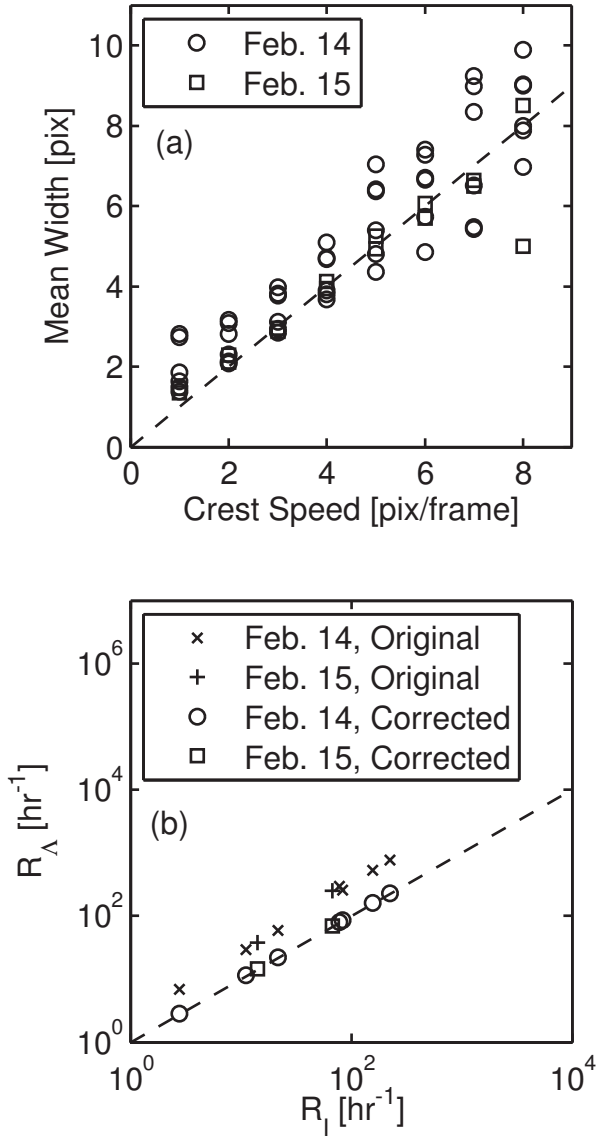


FIG. 15. (a) Comparison of mean crest width in pixels with crest advancement speed in pixels for both February 14 (circles) and February 15 (squares). (b) Comparison of calculated breaking rate from the first moment of $\Lambda(c)$, R_Λ , with the direct breaking rate R_I for the original distribution. R_Λ are shown without width correction (“original,” x’s for February 14, crosses for February 15), and with width correction (“corrected,” circles for February 14, squares for February 15).